Hotspot Swells Revisited

Scott D. King[a], Claudia Adam[a]

[a]*Department of Geosciences, Virginia Tech, Blacksburg, VA*

Abstract

The first attempts to quantify the width and height of hotspot swells were made more than 30 years ago. Since that time, global bathymetry, ocean-floor age, and sediment thickness datasets have improved considerably. Swell heights and widths have been used to estimate the heat flow from the core-mantle boundary, constrain numerical models of plumes, and as an indicator of the origin of hotspots. In this paper, we repeat the analysis of swell geometry and buoyancy flux for 54 hotspots, including the 37 considered by Sleep (1990) and the 49 considered by Courtillot et al. (2003), using the latest and most accurate data. We are able to calculate swell geometry for a number of hotspots that Sleep was only able to estimate by comparison with other swells. We find that in spite of the increased resolution in global bathymetry models there is significant uncertainty in our calculation of buoyancy fluxes due to differences in our measurement of the swells' width and height, the integration method (volume integration or cross-sectional area), and the variations of the plate velocities between HS2-Nuvel1a (Gripp and Gordon, 1990) and HS3-Nuvel1a (Gripp and Gordon, 2002). We also note that the buoyancy flux for Pacific hotspots is in general larger than for Eurasian, North American, African and Antarctic hotspots. Considering that buoyancy flux is linearly related to plate velocity, we speculate that either the calculation of buoyancy flux using plate velocity over-estimates the actual vertical flow of material from the deep mantle or that convection in the Pacific hemisphere is more vigorous than the Atlantic hemisphere.

Keywords: hotspot swells, depth anomalies, buoyancy flux, heat flow

1. Introduction

To first order, seafloor bathymetry can be explained by the cooling and sinking of a lithospheric plate as it moves away from a mid-ocean ridge (Turcotte and Oxburgh, 1967; Sclater and Francheteau, 1970). However, regionally bathymetric features can depart from subsidence models describing this conductive cooling (Parker and Oldenburg, 1973; Parsons and Sclater, 1977). A depth anomaly map (Figure 1) can be created by removing a theoretical depth provided by models of thermal subsidence of the lithosphere from observed sea floor topography (Menard, 1973; Crough, 1983; Marty and Cazenave, 1989; Davies and Pribac, 1993; Ito and van Keken, 2007). In Figure 1, areas in orange and white within the ocean basins represent ocean floor that lies more than 500 meters above the depth predicted by the depth-age curve of Parsons and Sclater (1977). Focusing on Hawaii, there is a thin white line of islands and seamounts and a much broader orange anomaly following the trend of the seamount from the Big Island of Hawaii to the bend in the chain at Midway Island. This anomalously shallow sea floor is the depth anomaly including both the hotspot swell and the volcanic islands/seamount, following the trend of the Hawaiian Island chain in the direction of motion of the Pacific plate. Topographic anomalies of different spatial length scales ranging from volcanic edifices (≈100 km) and swells around volcanic chains (≈1000 km)(Wilson, 1963; Morgan, 1971), to regions such as the South Pacific and African superswells that extend for several thousand kilometers (e.g., McNutt and Fischer, 1987; Gurnis et al., 2000).

Hotspots are regions of anomalous volcanism that appear to be unrelated to plate boundary processes (Wilson, 1963). While they are often far from plate boundaries, a number of anomalous regions along mid-ocean ridges, such as Iceland, Galapagos, and the Azores, are also classified as hotspots (Figure 1). Morgan (1971) proposed that the origin of hotspots is deep mantle plumes, although alternative theories including tensional fracture (Turcotte and Oxburgh, 1973; Stuart et al., 2007), lithospheric reheating (Detrick and Crough, 1978; Crough, 1978), small-scale convection (Vogt, 1991; King and Anderson, 1995, 1998; King and Ritsema, 2000), top-down tectonics (Anderson, 2001, 2002), remelting of slab material (**?**), and shear-driven instabilities (Ballmer et al., 2013) have also been proposed. The purpose of this paper is not to review or critique theories of hotspot formation, but to focus on the measurements of hotspot swells. We refer the reader to reviews focusing on hotspot geochemistry (White, 2010), geodynamics (Ito and van Keken, 2007; Burke, 2011), seismology (Li et al., 2003; Montelli et al., 2006; Boschi et al., 2007; Courtier et al., 2007) and geology (Morgan and Phipps Morgan, 2007) for aspects of hotspots that are not related to hotspot swells.

An updated compilation of hotspot swell geometry (i.e., height and width) will be useful for a variety of applications. The height and width of hotspot swells have been used to constraint numerical models of hotspot origin (e.g., Ribe and Christensen, 1999; Ito et al., 1997; Phipps Morgan, 1997; Stein-

Email addresses: sdk@vt.edu (Scott D. King), ca3@vt.edu (Claudia Adam)

berger, 2000; Lin and van Keken, 2006; Albers and Christensen, 1996; King and Redmond, 2007). Hotspot swells have been used to estimate the flux of material from the core-mantle boundary via plumes (i.e., buoyancy flux) and used this flux of material to estimate the amount of heat transported from the core-mantle boundary to the surface (e.g., Davies, 1988; Sleep, 1990; Hill et al., 1992). Additionally, updated swell geometry measurements may help to distinguish between hotspots associated with mantle plumes and those formed by shallower processes (Courtillot et al., 2003; Anderson, 2005).

The first compilation of hotspot swells reported swell heights ranging from 500-1,200 m and swell widths ranging from 1,000-1,500 km (Crough, 1983) with depth-anomaly values estimated to be accurate to roughly ±200 m. Davies (1988) estimated mass fluxes from 26 hotspot swells (Table 1,2), using the swell heights compiled by (Crough, 1983) and assuming a width of 1000 km for all hotspot swells. The cumulative buoyancy flux for the 26 hotspot swells computed by Davies (1988) was 41.3 Mg s^{-1}. Multiplying by the specific heat (1.25×10^3 J kg^{-1} $°C^{-1}$) and dividing by the coefficient of thermal expansion (3×10^{-5} $°C^{-1}$) he arrived at an estimate of total heat output from hotspots of 1.7 TW. Hill et al. (1992) revised this plume heat flux to 3.5 TW by considering time-averaging effects. They compared this 'plume flux' with an estimate of the global heat flux (44 TW) less the heat from continental radioactivity (8 TW) concluding that the mantle is 90% internally heated and 10% heated from the core.

Sleep (1990) considers 37 hotspots (Table 1,2), including on-ridge hotspots that were omitted by Davies (1988). A number of these were estimated based on limited data. Moreover, he calculated the buoyancy flux for the entire Pacific superswell and equally divided the result between Pitcarn, Marquesas, Macdonald, and Tahiti (e.g., 3.3 Mg s^{-1}). He noted that there is no obvious swell for Caroline, Samoa, Juan Fernandez, and San Felix and assigned half the buoyancy flux of the first group south Pacific of hotspots to these (e.g., 1.7 Mg s^{-1}). Both swell and volcanic activity at Louisville were even smaller than Caroline, Samoa, Juan Fernandez, and San Felix and he assigned these hotspots an upper limit of 0.9 Mg s^{-1} accordingly. Noting that Juan de Fuca and Bowie were both near the Juan de Fuca ridge and were visibly smaller than the Galapagos hotspot with ill-defined chains, lacking anomalous geochemical signatures, Sleep again assigned buoyancy flux values of 0.9 Mg s^{-1} to Juan de Fuca and Bowie. In the Atlantic, upper limits of 0.5 Mg s^{-1} were assigned for Fernando, Martin, Discovery, Meteor, and St. Helena because the swell evidence was inconsistent (Crough, 1983; Hayes, 1999). Finding it difficult to separate the elevation anomaly associated with the Kerguelen plateau from the current location of volcanism, Sleep assigned the buoyancy flux from Crozet to Kerguelen.

In the end, of the 37 hotspots considered by Sleep (1990) only 7 were identified as having good reliability, while 14 were ranked fair and 16 were ranked 16 poor (Table 2). Taking all 37 hotspots, Sleep (1990) calculated a mass flux of 54.9 Mg s^{-1} with the mass flux from the seven hotspots ranked good contributing 16.4 Mg s^{-1} and the 21 hotspots ranked good or fair contributing 41.7 Mg s^{-1} to the total buoyancy flux. These numbers compare with Davies (1988) total of 41.3 Mg s^{-1}. The spread in these numbers provides one measure of the uncertainty of the global buoyancy flux.

The initial motivation for this work was to determine to what extent modern global relief models could improve the assessment of hotspot swells and buoyancy fluxes. For several of the hotspots Sleep (1990) refers back to Crough (1983) for swell measurements, so a number of the estimates of swell geometry are based on observations that are more than 30 years old. In the following sections we describe the datasets and methods we use to measure hotspot swell geometry, compare our results using two independent measurement methods, and compare our updated results with the historical compilations described above. In the online supplement, we provide maps and cross sections for each of the hotspots we studied, allowing the reader to make their own independent evaluation of our measurements.

2. Method

When undertaking a global survey of hotspots, the first issue one is confronted with is which compilation of hotspots to use. Davies (1988) considered 26 locations, Sleep (1990) considered 37 locations, Steinberger (2000) considered 44 locations, Courtillot et al. (2003) considered 49 locations, Anderson (2005) considered more than 60 locations and Ito and van Keken (2007) consider 69 locations, although Ito and van Keken (2007) do not identify active volcanism for all these locations. The buoyancy flux values from Davies (1988) and Sleep (1990) are reproduced in Table 2 along with locations taken from Courtillot et al. (2003). Other compilations including **?**, Turcotte and Schubert (2002) and rely on Courtillot et al. (2003) previous compilations, mainly Sleep (1990). We choose to analyze 54 hotspots including all those used by Sleep (1990) and Courtillot et al. (2003) (Table 1).

Calculating a depth anomaly map is common to all of the three methods we design to compute the bouyancy flux. In the ocean, we create a depth anomaly map by taking a gridded topographic relief model and subtracting a model of the bathymetry based on the a square-root of age,

$$psm(\theta,\phi) = -2500.0 - 350\sqrt{0.01t(\theta,\phi)} \quad t < 70\text{My} \tag{1}$$

$$psm(\theta,\phi) = -6400.0 + 3200\exp\left[\frac{-0.01t(\theta,\phi)}{62.8}\right] \quad t \geq 70\text{My} \tag{2}$$

where $psm(\theta,\phi)$ is the model bathymetry in meters and $t(\theta,\phi)$ is the age of the ocean floor in millions of years (Parsons and Sclater, 1977). For the observed topography we use ETOPO2, which has a spatial resolution of 2 arc-minute and a vertical accuracy on the order of 10 meters. We take the age of the ocean floor from Müller et al. (2008). We then correct the bathymetry for sediment loading using Whittaker et al. (2013), where sediment thickness values are averaged over 5-arc-minute grid cells. The resulting depth anomaly, da, is given by:

$$da(\theta,\phi) = topo(\theta,\phi) - psm(\theta,\phi) + \left[\frac{\rho_s - \rho_m}{\rho_m - \rho_w}\right] sed(\theta,\phi), \tag{3}$$

where $topo(\theta,\phi)$ is the gridded topography, $psm(\theta,\phi)$ is given in equations (1) and (2) and $sed(\theta,\phi)$ is the sediment thickness

map, ρ_m is th density of the mantle (3.3×10^3 kg m^{-3}), ρ_s is th density of sediment (2.3×10^3 kg m^{-3}), and ρ_w is th density of water (1.0×10^3 kg m^{-3}). On land, we apply no corrections to the topography; the depth anomaly is assumed to be the same as the topography. For illustration, the resulting global depth anomaly map is shown in Figure 1.

We quantified the buoyancy fluxes while using the Parsons and Sclater (1977) model of the thermal subsidence of the lithosphere (PSM hereafter). Indeed, because our goal was to compare our new estimations to Sleep (1990)'s results, we tried to choose parameters which are the closest to those. However, the choice of thermal subsidence model of the lithosphere also introduces some uncertainties. Adam and Bonneville (2005) show that the amplitude of the South Pacific superswell is 100 m higher when quantified with the PSM model than when quantified using the GHD1 model (Stein and Stein, 1992). In terms of buoyancy flux, this introduces a difference of 17%; the buoyancy fluxes computed with GDH1 and PSM being 11.3 and 16.2 Mg s^{-1} respectively. A similar difference (16%) was reported for Hawaii (Vidal and Bonneville, 2004), where the buoyancy fluxes computed with GDH1 and PSM are 3.4 and 4.7 Mg s^{-1} respectively. For Tristan and the African superswell, we find in this study that the choice of the subsidence model induces an error of 8.2 % and 5.2% respectively.

However, the difference induced by the choice of the thermal subsidence of the lithosphere is not systematic. Indeed, for the characterization of the swells located on the south Pacific superswell we have removed the long-wavelength component of the superswell, so the choice of the subsidence model will not affect the determination of these buoyancy fluxes. For chains located near the continental shelf (such as Cape Verde, Canaries, Fernando), the general trend of the bathymetry is not well reproduced by the classical subsidence models. The seafloor is indeed becoming shallower while approaching the continent, instead of deepening as a function of age, as the subsidence models predict.

Several models have been published since PSM and GDH1 (Stein and Stein, 1992) including Doin and Fleitout (1996), Hillier and Watts (2005), Korenaga and Korenaga (2008) and Hillier (2010). However, all seafloor subsidence models have difficulty near the continental slope, where a significant fraction of hotspots occur. To illustrate, we plot PSM along with GDH1 and our hotspot elevation measurements (described below) in Figure 3. The mean depth for the Geometrical approach has been obtained by taking the mean of the depth anomaly in a 5 degree by 5 degree box, whereas for MiFil, we take the mean value in 500 km diameter circle. At seafloor ages >80 Myr, which is the case for many hotspots in the Atlantic, the difference between the hotspot depth anomaly and the sea floor subsidence becomes increasingly large and is not accounted for by any sea floor subsidence model. For younger ages, we also find noticeable departures between the models estimations and ours.

2.1. Geometrical Measurement of Swell Cross-sectional Area

After calculating the residual depth anomaly, we remove the average value of the depth anomaly from a 5 degree by 5 degree area surrounding the hotspot (both for hotspots on land or ocean) and this mean value is reported on each figure. We then project the modified depth anomaly onto a profile perpendicular to the direction of plate motion, using the HS3-nuvel1a (Gripp and Gordon, 2002) velocity model centered at the maximum height of the depth anomaly. Generally the maximum depth anomaly does not correspond to the active volcanism, for which latitude and longitude values are given in Table 1. The latitude and longitude used in the depth anomaly calculation for each hotspot are reported on the figure. For illustration, the depth anomaly map and projected profile for Hawaii are shown in Figure 4. The red line is a bi-quadratic fit to the depth anomaly within the circled region on the map. The radius of the circle is determined by trial and error, comparing both the map and the cross-sectional profile to visually obtain the best fit. We then determine the swell height by taking the maximum minus the minimum points of the bi-quadratic fit. Because we have removed the mean depth in the region around the hotspot, it would be incorrect to measure the depth anomaly as the height above the zero depth. In a few cases, notably Arago, East Africa, Eifel, and Meteor, the method breaks down because short-wavelength features in the profile dominate the quadratic fit. Maps and profiles for all of the hotspots are provided in the online supplement.

The approach described above is one of three approaches described in Sleep (1990) and is nearly identical to the approach used by Davies (1988). We do not use the spreading ridge approach described by Sleep (1990) for Iceland or any other on-ridge hotspot or the approach for a stagnent plate, applied to Cape Verde, which uses the geoid. We apply geometrical approach described above to all hotspots in order to obtain an estimate the width and height of the depth anomaly.

In addition to the choice of reference model in the calculation of the depth anomaly, there are several other challenges. First, it is difficult to identify the maximum of the swell height because the swell height has a contribution from the island and/or seamounts in addition to the swell (Wessel, 1993). The assumption that is generally made in this type of analysis is that the wavelength of this topography is short enough that it is primarily supported by elastic flexure, while the wavelength of the swell is long enough to be supported primarily by isostacy (Wessel, 1993). McNutt and Shure (1986) assumed that the swell geometry at Hawaii was caused by a low-density subsurface load and modeled both the swell geometry and flexural response using an approach using linear filters. This approach is only applicable if the origin of the swell is shallow. We use a quadratic fit to the regional depth anomaly, Crough (1978) used a Gaussian function and Wessel (1993) used a super-Gaussian function to study the Hawiian swell. Second, as discussed previously, it is hard to define the mean ocean depth for hotspots that are located near a continent boundary. The problem is illustrated by the residual depth anomaly plots for Cape Verde (Figure 5). It is difficult to identify the regional topographic trend in this region because the continental shelf/continental slope is directly to the east of Cape Verde and there is a shallow platform to the WNW. Finally, some hotspot swells are not actually swells but are large plateaus. This is best illustrated by

comparing the residual depth anomaly plots for Kerguelen (Figure 6) with those for Hawaii (Figure 4). Whereas hotspot swells have a Gaussian (Crough, 1978) or super-Gaussian (Wessel, 1993) shape, Kerguelen is an oceanic plateau that is thought to have formed when the hotspot interacted with the ridge. The steep sides of the plateau do not resemble other oceanic hotspot swells.

We report swell geometry and buoyancy flux without attempting to correct for local and/or regional geology. For cases such Cape Verde and Kerguelen described above, the concerns may be somewhat obvious from the figures but for other hotspots there may be less apparent issues that will be apparent to researchers familiar with the area. We do not want to intraject our own biases into the compilation and encourage the reader to examine the plots in the supplemental material and make their own judgements.

Because of challenges that we identified using the geometrical procedure, the approach used by Davies (1988) and Sleep (1990), we compare the geometrical procedure results with the MiFil approach (Adam et al., 2005).

2.2. MiFil Volume

The MiFil method (for minimization and filtering) is a filtering method especially designed for the characterization of depth anomalies (Adam et al., 2005). The MiFil method requires two stages: the first is to approximately remove the island/volcanic component of topography by minimizing the depth anomaly and then to smooth the shape and totally remove the remaining small spatial length scale topography due to seamounts and islands using a median filter. The strength of this method is that it does not require any assumption on the location, amplitude, or width of the large-scale feature to characterize. The filtering parameters, i.e. the radii of the minimizing and median filters, are computed by considering the spatial length scale of the features to remove: the islands and seamounts.

Previous computations of the buoyancy fluxes through the MiFil method (Vidal and Bonneville, 2004; Adam et al., 2005, 2007) do not use the swell's width and amplitude along depth cross sections and instead consider the swell's volume encompassed in a box elongated along the direction of the plate motion, between the swell's maximum and the active volcanism. The velocities considered in these previous studies are either mean velocities in the study area (110 mm/yr for French Polynesia for example for Adam et al. (2005)) or velocities deduced from the spatial distribution of the volcanism ages (Vidal and Bonneville, 2004; Adam et al., 2007). We illustrate the MiFil approach for the Hawaiian swell in Figure 7 in order to allow the reader to compare with the Geometrical approach in Figure 4. The maps of swells and cross-section plots obtained using the MiFil approach for the other hotspots are included in the supplemental data.

The challenge with using the MiFil approach in the present study is that not all swells have present day volcanism. Bermuda is an excellent example because the most recent volcanic activity on the Bermuda swell is dated at 33 Ma (Tucholke and Vogt, 1979) and at the projection of the hotspot track to the present day location of the hotspot there is no evidence of anomalous volcanism (Vogt and Jung, 2007). In this case we make up a active volcanism point, coherent with the swell morphology and the plate's velocity using the HS3-Nuvel1a plate model. Moreover, we rescale the previous results published with MiFil when other plates' velocities have been considered.

2.3. MiFil Area

The final approach used to characterize the swells morphologies uses the depth anomaly filtered through the MiFil method to obtain the swells' width and amplitude in a way similar to the geometrical method. We look along profiles perpendicular to the plate motion direction to derive these parameters. The main difference is that, as the volcanoes or other short wavelength anomalies have already been removed through the filtering process, we do not have to fit by a gaussian or other geometrical method. The swell parameters are derived directly along the depth cross section going through the swells' maximum.

2.4. Buoyancy Flux

Both the Geometrical and MiFil-area methods described above can be used to compute the cross-sectional areas of hotspot swells. In order to convert these areas to buoyancy flux, we follow the approach described by Sleep (1990), who shows that the buoyancy flux necessary to maintain a swell is given by

$$B = W\overline{E}(\rho_m - \rho_w)V_L = \overline{\delta\rho_p}Q_p, \tag{4}$$

where W, the width of the swell perpendicular to the plate direction, $\overline{E}$, the excess elevation averaged across the swell, ρ_m, the mantle density, ρ_w, water density, V_L, the plate velocity in the hotspot frame, $\overline{\delta\rho_p}$, the average density reduction in volume flux per time, and Q_p, the volume flux of material supplied to the plume. The product $W\overline{E}$ is the cross-sectional area. It is worth emphasizing that the swell width, W, mean swell height, E, and plate velocity, V_L, do not require the existence of a mantle plume. Multiplying Davies (1988) swell magnitude by $(\rho_m - \rho_w)$ gives the buoyancy flux defined by Sleep (1990). For the cases of hotspots on land (e.g., Afar, Australia, Baja, Eifel, Hoggar, Raton, Tibesti, and Yellowstone) we use ρ_m as opposed to $(\rho_m - \rho_w)$ for the density. Whereas Davies (1988) uses 75% of the maximum swell height as the average, we note that many swells have a nearly sinusoidal shape and we use $\frac{1}{\pi}\int_0^{\pi}\sin(x)dx = \frac{2}{\pi} = 0.64$. Hence using 0.75 produces a buoyancy flux estimate that is larger than the area under the swell.

3. Comparison Between Approaches

In order to assess the uncertainty in measurement of swell geometry we independently measured hotspot swells from the 54 hotspots (Table 1) using the cross-sectional area, MiFil area MiFil volume approaches (Table 3).

Located far from a ridge, continental shelf, fracture zone, plateau or other swell, Hawaii is the type example of a hotspot swell that is consistent with many of the predictions of a mantle plume interacting with a plate. Even so, estimating the buoyancy flux from Hawaii is not without uncertainty. Here one of the sources of uncertainty is the velocity of the Pacific plate

(Table 4) which ranges from 86 mm yr^{-1} from Gordon and Jurdy (1986) (used by Sleep (1990)) to 104.3 mm yr^{-1} from Gripp and Gordon (2002) (HS3-Nuvel1a), a difference of almost 20%. The swell cross-sectional area estimated by Sleep (1990) is 1430 km^2, while Davies (1988) estimated 900 km^2, a difference of more than 35%. Based on the Geometrical approach (Figure 4) we estimate a cross-sectional area of 954 km^2, while using the MiFil approach (Adam et al., 2005) we obtain 1453 km^2. As a result, while Sleep (1990) calculates a buoyancy flux of 8.7 Mg s^{-1} and Davies (1988) calculates a buoyancy flux of 6.3 Mg s^{-1}, we calculate a buoyancy flux of 4.7 Mg s^{-1} using the Geometrical approach and 4.9-7.1 Mg s^{-1} using the MiFil-volume and area methods (Vidal and Bonneville, 2004). We use Gripp and Gordon (2002) (HS3-Nuvel1a) throughout unless otherwise specified. While for the Pacific plate the magnitude of the plate velocity changes and the direction does not, for the African plate both the magnitude and direction change significantly (Table 4).

We plot the swell width (Figure 8a) and height (Figure 8b) from the Geometrical approach against swell width and height from the MiFil-area method. The measurements cluster along lines with a slope of 1 with R^2 values of 0.41 (width) and 0.35 (height). These low values of R^2 raise some concern about the reliability of our measured swell heights and widths. There is less scatter in the width measurements than the height measurements and in general, the widths as measured by the Geometrical method tend to be larger than those measured with the MiFil method. The standard deviation of the two measurement fits is 179 km for the width and 440 m for the height. We take these as quantitative measures of the uncertainty of our measurements. The scatter of the measurements for small swells is not surprising and reflects our attempts to measure swell geometry near the limit of our measurement uncertainties. The swells that are the largest outliers in width are Azores, Cape Verde, Hoggar, and Kerguelen, while the largest outliers in height are Afar, Cape Verde, and Jan Mayen. The geometrical approach tends to have larger widths while the MiFil approach tends to have larger swell heights. Because the buoyancy flux is the product of width and height, we also plot the product of width and height (Figure 8c), and the R^2 value is 0.62 and the standard deviation 235 km^2. This reflects the tradeoff between width and height (you can often fit a swell with a greater width and lower height or a narrower width and a greater height) and difference in the researchers choice of whether to focus more on width or height.

For Cape Verde there is a significant regional bathymetry variation and identifying the reference bathymetry is challenging. For Kerguelen it is unclear how much, if any, of the plateau should be included. We note that there is a similar degree of difference between the buoyancy flux calculations of Davies (1988) and Sleep (1990). Because Davies (1988) assumes a uniform swell width and Sleep (1990) assigns many values without measurement, we do not attempt to analyze their measurements.

In Figure 9a we plot the buoyancy flux obtained through the cross-sectional area method. We plot the average value of the buoyancy fluxes calculated from the Geometrical and MiFil-area approaches (Table 3) and the error bars represent the uncertainty induced by the estimation of the swell width and height (i.e., the difference between the measurements from the two approaches). In Figure 9b we plot the uncertainty in buoyancy flux as a percent error. The hotspots are plotted in alphabetical order along the x-axis (Table 1).

It is clear from Figure 9 that swells with large cross-sectional areas have smaller uncertainty than those with small cross-sectional areas. The uncertainty reflects the difficulty in quantifying the anomaly. The large volume swells associated with small uncertainty with the cross-sectional area determination are Hawaii, Iceland, Macdonald, Marquesas, Rarotonga, and Society. There are actually some smaller swells which are also associated with a small uncertainty with the cross-sectional area determination: Ascension, Baja, Bermuda, Darfour, Easter, Fernando, Galapagos, Reunion, and Tibesti. Of these hotspots, Sleep (1990) assigned Bermuda, Hawaii, Iceland and Reunion 'good' reliability, while Easter, Galapagos, Macdonald, Marquesas, and Society/Tahiti were assigned 'fair' and Baja and Fernando were assigned 'poor' (Table 2). Thus the hotspots we identify with the smallest uncertainty include examples from all three of Sleep's subjective reliability catagories and Afar and Crozet, which Sleep identified as good, did not have a small uncertainty in our analysis.

To further illustrate the uncertainty in the measurements, we plot the swell cross-sectional area from Davies (1988) versus our measurements from the Geometrical method in Figure 10a. With the exception of Kerguelen and Fernando, all of the points plot near or below a line with a slope of 1, indicating that Davies (1988) cross-sectional areas are systematically larger than ours. Because Davies assumes that all swells have a width of 1,000 km and our measured swell widths range from 100–1,100 km, it is not surprising that for many swells our cross-sectional areas are significantly smaller than Davies (1988). The cross-sectional areas of three of the largest swells (e.g. Hawaii, Discovery and Pitcairn) all fall close to the one-to-one line on Figure 10a and for these swells we measure swell widths close to Davies' assumed width. Kerguelen is problematic as we have discussed above, and separating the plateau and swell is no trivial. Because the cross-sectional area is the swell width times height, in order to address whether the swell widths are the cause of the difference between our results and Davies, we also plot our measured swell heights versus those from Davies in Figure 10b. The swell height measurements (Figure 10b) scatter about a line with a slope of 1 with as many points above as below and we observe no systematic trend, confirming that Davies (1988) assumed uniform swell width of 1,000 km for all hotspot swells leads to a systematic over-estimate of cross-sectional area and hence buoyancy flux.

The influence of the velocity variation between the different kinematic models is illustrated in Figure 11. In Figure 11a we plot the average buoyancy flux calculated using the Geometrical approach with HS2 and HS3 velocities. The error bars represent the uncertainty induced by the difference between the HS2-Nuvel1a and HS3-Nuvel1a plate velocity at each hotspot. In Figure 11b we plot the uncertainty in buoyancy flux due to the difference in plate velocity as a percent error. Once again,

the hotspots are plotted in alphabetical order along the x-axis (Table 1). HS2-Nuvel1a is based on Cenezoic hotspot locations while HS3-Nuvel1a is based on measurements for the past 4-7 Myrs. For the Pacific and North American plates, the difference between HS2-Nuvel1a and HS3-Nuvel1a is primarily magnitude, while for the African and Antarctic plates, the direction also differs. The results are similar to Figure 9a with Hawaii, Iceland, Macdonald, Marquesas, Rarotonga, Samoa, and Society/Tahiti having the largest buoyancy fluxes and the smallest uncertainties. Davies (1988) used Pollack et al. (1981) for plate motions in a hotspot reference frame where Pollack et al. (1981) rotated the Minster and Jordan (1978) plate model into a hotspot reference frame. Sleep (1990) used plate motions from Gordon and Jurdy (1986), which for the Pacific plate are about 10% slower than Pollack et al. (1981). The values of plate velocity for Hawaii for all for plate models, which are representative of the variation in plate velocity for all of the Pacific hotspots, are presented in Table 4. However, hotspots on the African plate have the largest uncertainty in buoyancy flux due to the difference between HS2-Nuvel1a and HS3-Nuvel1a (Table 4 and Figure 11).

3.1. Comparison Between Geometrical, MiFil-area and MiFil-volume approaches

Other uncertainties are introduced by the method employed for computing the buoyancy fluxes. Sleep (1990), the Geometrical and the MiFil-area approach use equation 4 where the swell's width and height are estimated along depth cross sections, whereas the MiFil-volume approach consider the swell's volume encompassed in a box elongated along the direction of the plate motion, between the swell's maximum and the active volcanism. This approach is also discussed by Sleep (1990); however he used cross-sectional areas for most of his measurements. The difference between the buoyancy fluxes computed through the volume integration, B_{vol}, and through the depth cross-sectional area, B_{area}, both obtained after filtering with MiFil, is shown in Figure 12. There appears to be a linear trend with some of the largest buoyancy fluxes, including Louisville, Society and Hawaii lying along a line with a slope of 1.45. If the swell's morphology corresponds to the classical definition of a plume lithosphere interaction (Sleep, 1990; Ribe and Christensen, 1999), one would expect all the swells to fall along a line which slope is slightly greater than one. Indeed, the volume computed through the cross-sectional area method is greater than the volume integrated along the hotspot track, because the volume integration method takes into account the variation of the swell morphology, whereas the cross-sectional area method considers the maximum values of the swell's width and amplitude. However, the morphologies of hotspot swells can be quite irregular. The fact that the swell's maximum is located far from the active volcanism along the Austral chain, explains the departure of Macdonald from this linear trend. The peculiar shape of swells' morphology also accounts for the departure of Marquesas from the linear trend. The other main outliers are Easter, Caroline, Kerguelen and Samoa. For these latter B_{vol} is indeed much bigger than B_{area}. Some of these departures can be accounted for if one considers their geological contexts. For example Easter is near the triple junction and there is a hotspot track on two plates while Kerguelen is a plateau and does not fit the classical swell model. The computation of the buoyancy fluxes for Iceland and Afar through the volume integration method uses the relative velocities of the two lithospheric plates where these two hotspots are, whereas the depth cross-sectional area uses the HS3-Nuvel1a reference frame. Considering how different the parameters used for both computations are, the final correlation is actually rather good.

The total uncertainty associated with all the parameters previously described (swell's width and height, plate velocity, area or volume methods) is represented in Figure 13. We find a pattern similar to Figures 9 and 11 with somewhat larger error bars. We note that aside from Iceland, the other hotspots with the largest buoyancy fluxes are on the Pacific plate. Recalling the earlier estimate that the difference between removing PSM versus GDH1 to create a residual anomaly map resulted in of order 15% difference in buoyancy flux for Hawaii and the Pacific superswell, 8% for the African swell, 5.2% for Tristan and less than 5% for all other swells, the reference model is not the largest source of uncertainty in the calculation of buoyancy flux.

In Figure 14, we plot the correlation between buoyancy fluxes from Sleep (1990) and our results obtained through the volume integration method using the kinematic velocities from the HS3-Nuvel1a plate model. Some of the hotspots with the largest buoyancy fluxes, including Samoa, Society, and Hawaii lie along a line with a slope of 1.6 and thus the values we compute are generally smaller than those computed by Sleep (1990). This is understandable because our method takes into account the spatial variation of the swell morphology, whereas the cross-sectional area method used by Sleep (1990) considers the maximum values of the swell width and amplitude. Moreover the kinematic velocities used in both models are also different (e.g., Table 4). However, there appears to be a consistent trend for the largest swells. For the other hotspots located in the south Pacific, Sleep (1990) estimated the superswell contribution and then distributed it equally between the chains. Because our study considers each chain separately, it is hard to make a quantitative comparison with Sleep's results. Afar and Iceland have been obtained through completely different methods and thus it is not so surprising that our estimations are not in good agreement. Furthermore, Sleep (1990) does not compute a value for Kerguelen but assigns it the same value he found for Crozet and this can account for the departure we observe. This is an example where even though we have improved data and an improved method, we encounter the same problem as Sleep.

3.2. Buoyancy Flux and Heatflow

Following Davies (1988) and Sleep (1990), we sum our buoyancy fluxes (Table 3) and find a cumulative buoyancy flux of 36.75 Mg s^{-1} for the Geometrical method, 29.95 Mg s^{-1} for the MiFil-area method and 23.13 Mg s^{-1} for the MiFil-volume method. These are smaller than Davies (1988) cumulative flux of 41.3 Mg s^{-1}. As indicated previously, it is not surprising that our values are smaller than Davies (1988) because we do not assume a 1000 km swell width for all hotspot swells; most of our

measured swell widths are less than 1000 km. Our cumulative buoyancy flux values are also smaller than the 54.9 Mg s^{-1} calculated by Sleep (1990). We note that Sleep calculates a buoyancy flux for the entire superswell and distributes this across five hotspots. If we add the buoyancy flux for the Pacific superswell, which we calculate to be 16.2 Mg s^{-1}, a buoyancy flux contribution for the African superswell, which we estimate to be 0.7 Mg s^{-1}, following the approach used by Gurnis et al. (2000), our cumulative buoyancy flux values are 53.65 Mg s^{-1} for the Geometrical method, 46.85 Mg s^{-1} for the MiFil-area method and 40.03 Mg s^{-1} for the MiFil-volume method. We note Sleep does not explicitly account for the African superswell.

If we multiply by the specific heat (1.25×10^3 J kg^{-1} $°C^{-1}$) and divide by the coefficient of thermal expansion (3×10^{-5} $°C^{-1}$), we arrive at estimates of total heat output from hotspots and the Pacific and African superswells of 1.67–2.23 TW, giving a mean value of 1.95±0.28 TW, (or a 14.5% uncertainty). These variations could have significant implications when used as parameters in other quantitative models. The range of total heat output is consistent with the values from Davies (1988) of 1.7 TW and Sleep (1990) of 2.3 TW. Overall our total heat flux resulting from swells is consistent with previous estimates because the largest uncertainties in our calculations are for the smaller swells which do not contribute significantly to the total heatflux.

We note that Malamud and Turcotte (1999) estimated that there are nearly 5000 plumes based on assumed statistical distribution of plume sizes, and suggested that Davies (1988) and Sleep (1990) may have significantly under-estimated CMB heat flux. Leng and Zhong (2008) showed clearly that in compressible mantle convection, plume heat flux in the upper mantle as constrained by swell buoyancy flux is probably only 1/3 of the core mantle boundary heat flux, due to the effect of adiabatic heating. Thus even with improved constraints on swell geometry the resulting estimates of heat flux are significantly uncertain due to other factors.

3.3. Comparison with Other Hotspot Observations

The focus of this review has been hotspot swells and an exhaustive literature review for each hotspot is beyond the scope of this review. We refer the reader to recent reviews by Anderson (2005),Morgan and Phipps Morgan (2007), Ito and van Keken (2007), White (2010), and Burke (2011).

It is interesting to compare our results with other observations related to hotspots. Courtillot et al. (2003) classify hotspots using five criterion: long-lived tracks, large igneous provinces (traps) at the initiation of the chain, buoyancy flux value in excess of 1 Mg s^{-1}, a high He or Ne ratio, and slow shear wave velocity at 500 km depth. They identify nine hotspots that have at least three of the five characteristics: Hawaii, Easter, Louisville, Samoa, Caroline, Iceland, Afar, Reunion, and Tristan and then remove Samoa because it has a clear, short track without a flood basalt or oceanic plateau at the onset, and Caroline because they find neither a tomographic anomaly nor an associated flood basalt associated with the Caroline chain. Montelli et al. (2006) examine finite-frequency tomographic images of shear-wave velocity and argue for the existence of deep mantle plumes below: Ascension, Azores, Canary, Cape Verde, Cook Island, Crozet, Easter, Kerguelen, Hawaii, Samoa, and Tahiti with anomalies extending to at least the mid-mantle beneath Afar, Atlantic Ridge, Bouvet, Cocos/Keeling, Louisville, and Reunion.

Comparing the list of hotspots from these two studies with the hotspots with the largest buoyancy fluxes: Afar, Bermuda, Galapagos, Hawaii, Iceland, Louisville, Macdonald, Marquesas, Pitcairn, Samoa, and Society/Tahiti, we find surprisingly little overlap; only Afar, Hawaii, Louisville and Iceland are common to all three lists. We could also include Samoa if we compare with to Courtillot et al. (2003)'s original list of nine. We find the small overlap puzzling because we agree with Courtillot et al. (2003) that the five observations that they consider should be expected at hotspots resulting from deep mantle plumes based on numerical modeling of plumes (e.g., Richards et al., 1989; Ito et al., 1997; Lin and van Keken, 2006). Furthermore, the fact that several prominent swells (e.g., Bermuda and Marquesas) are likely the result of a process other than a deep mantle plume illustrates the importance of considering multiple working hypotheses with regard to swell origin.

While hotspot swells have been used as an indicator of a deep mantle plume by some authors, the presence of absence of a swell may not be a sufficient indicator of a deep plume. For example, the Marquesas Island chain departs from the trends of other south Pacific hotspot traces by 20-30° (McNutt et al., 1989; Brousse et al., 1990). Moreover, it has been demonstrated that most of the seafloor depth anomaly is explained by crustal underplating (McNutt and Bonneville, 2000) pointed out by seismic refraction experiments (Caress and Chayes, 1995; Wolfe et al., 1994). The anomalously thick crustal root is indeed a buoyant load that flexes the elastic plate upward from below, thus creating an important seafloor depth anomaly over the volcanic chain (Wolfe et al., 1994). This implies that an important swell and the inferred big buoyancy flux are not systematically representative of a buoyant upwelling of a plume. In addition, recent tomographic imaging shows that slow seismic velocities associated with the French Polynesia plumes, often extend to depths shallower than 200 km (Isse et al., 2006). This tomographic model has been obtained through the inversion of Rayleigh waves. Therefore depths greater than 220 km are not imaged. But among the six plumes imaged in the 0-220 km depth range, only three may be connected to deeper anomalies.

Bermuda is an elongated swell with the long axis of the swell inclined almost 30° to the direction of the North American plate in the HS3-Nuvel1a model and at nearly right angles to the no-net rotation Nuvel1a direction of the North American Plate (Benoit et al., 2013). Furthermore, the only dated volcanic material has an age of 33-40 Myr (Vogt and Jung, 2007). There is no trace of a swell either west of Bermuda or at the present day location of the Bermuda hotspot following HS2-Nuvel1a or HS3-Nuvel1a (Benoit et al., 2013). The Bermuda swell could be: 1) a secondary upwelling associated with small-scale convection in the upper mantle (Vogt, 1991; King, 2007; Benoit et al., 2013), or 2) a weak plume that is only expressed at the

fracture zone associated with Bermuda (Vogt and Jung, 2007), or 3) some other, as of yet undescribed process entirely. Both Bermuda and the Marquesas have clear, well-defined swells, yet a deep plume origin is not a certainty for either case.

3.4. Comparison with transition zone thickness

There have been a number of investigations of transition zone thickness using SS-precursors and receiver functions (Li et al., 2003; Benoit et al., 2006; Deuss, 2007; Suetsugu et al., 2007; Lawrence and Shearer, 2008; Gu et al., 2009; Helffrich et al., 2010; Benoit et al., 2013). Because the Clapeyron slope of the olivine to wadsleyite phase transition is positive and the Ringwoodite to perovskite plus ferropericlase is negative (e.g. Frost, 2008), a hot tail of plume material rising through the transition zone should produce a thinner transition zone (Courtier et al., 2007). We compare the transition zone thickness measurements (Li et al., 2003; Benoit et al., 2006; Deuss, 2007; Suetsugu et al., 2007; Lawrence and Shearer, 2008; Gu et al., 2009; Helffrich et al., 2010; Benoit et al., 2013) with our buoyancy flux measurements in Figure 15. There is a lot of scatter and a trend it not obvious. While many of the smaller buoyancy flux measurements have a large uncertainty, the larger buoyancy fluxes, which define the trend in the plot, have smaller uncertainties. Even if we exclude many of the buoancy fluxes less than 1 Mg s^{-1}, the scatter for Hawaii covers the range of transition zone thicknesses. With the exception of a few of the measurements from Deuss (2007), all the transition zone thickness measurements are thinner than the global average, as would be expected if the mantle beneath swells were hotter than average.

4. Conclusions

Using the latest and most accurate data, we estimate buoyancy fluxes for 54 hotspots (Table 3) and compute the uncertainty associated with our estimations by considering the uncertainties due to our measurement of the swells' width and height, the integration method (volume integration or cross-sectional area), and the variations of the plate velocities between HS2-Nuvel1a and HS3-Nuvel1a. The estimated uncertainties are large, on the order of 50-80% for the small swells, with smaller uncertainties for the largest swells. The largest buoyancy fluxes are found for Hawaii, Society, Macdonald, Iceland, Afar, Marquesas, Rarotonga, and Samoa. Ranking the largest to smallest buoyancy flux swells depends on model assumptions. e.g., volume integration versus cross-sectional area for example. However Hawaii is clearly the largest, regardless of the parameters used for the buoyancy flux computation. If we use the results of Albers and Christensen (1996), which indicate that a buoyancy flux greater than 1 Mg s^{-1} is necessary for a plume to reach the surface from the core mantle boundary, then all only the hotspots listed above have the potential to come from the core-mantle boundary. We have argued above that Marquesas is likely due to underplating and a deep plume is not necessary. In comparison with Courtillot et al. (2003), Easter, Louisville, Reunion and Tristan are absent from our list. For all four of these hotspots, the buoyancy flux calculated from all three methods would have to be doubled.

The large uncertainties that we calculate reflect the difficulty in identifying and isolating a swell for many hotspots. The problem is not a limitation of the available topographic or sedimentary data but instead points to the need for better reconstructions of the geologic history in the regions around many hotspots. While we have been tempted to suggest that some, indeed many, of these hotspots are not the result of plumes we do not feel this could be strongly justified based solely on measurements of swell geometry. Even studies taking more factors into account do not reach the same conclusion regarding potential deep mantle sources for hotspots (Courtillot et al., 2003; Anderson, 2005). More careful modeling of plume lithosphere interactions, including proper thermodynamics of melting, would be useful to address whether it is possible to have a plume interact with the lithosphere producing no discernible swell.

We find it interesting that many of the largest swells occur on the Pacific plate, which is also the fastest moving plate. If for example, one assumes that swells are the result of mantle plumes and that all plumes were roughly the same size no matter where they were located, one would expect the largest swells over the slowest moving plates. Either something is missing in our understanding of buoyant mantle interacting with stagnant or mobile plates or convection in the Pacific is significantly more vigorous than under the Atlantic hemisphere.

Another intriguing observations is that the continental swells are generally much smaller than the oceanic ones. In fact for most of them we are not even sure that the depth anomaly we characterize is actually a swell, created by buoyant mantle upwellings, from which we can extract heat flow values, or accumulation of volcanic material (especially on slow moving plates such as Africa). Further studies based on seismic and gravity data could help to address this problem. The dynamic upwelling of plumes (or other buoyant mantle anomalies) should create a swell of greater width and smaller amplitude in the continental context, because the elastic thickness is larger than for oceanic lithosphere. The processes of plume/lithosphere interaction seem to be completely different from continents to oceans. Some studies show that the local stresses induced by melting under the continental lithosphere impede the upwelling of magma to the surface and instead favors the creation of dykes and sills (Grégoire et al., 2006). Another intriguing and non-classical example of the plume lithosphere interaction in the continental context is Yellowstone, where the volcanic chain lies on a topographic low, which has been interpreted by some authors as the delamination of the lithosphere by the plume (Ribe and Christensen, 1994). It seems then that the structure of the lithosphere plays a major role in the swell characteristics. Deriving heat flow from a swell without understanding the processes at its origin seems risky. Previous studies (e.g., Crough, 1983) have pointed out a correlation between the swell morphology and the age of the oceanic lithosphere. Our results do not find a correlation with age of the lithosphere. We mainly point out a distinct behavior for the different tectonic contexts.

Further progress in understanding hotspot origin will require integrated studies that include careful consideration of the regional geology. The differences between the results we calculate using different methods does not reflect a limitation in the

data and has much more to do with subjective choices by the researcher. Very few hotspots look like Hawaii. Many hotspots intersect fracture zones, cross ridges, or are near the contiential slope. Filtering techniques cannot isolate every feature and the estimate of the mean depth in the vacinity of a hotspot is a subjective process.

Fundamental studies aiming to understand the plume initiation and the plume/lithosphere interaction processes are necessary. However, local studies based on data also bring insightful constraints on the processes involved in the plume/lithosphere interaction. In particular, recent models based on tomography models have proven to provide an accurate description of the surface observations (Ghosh and Holt, 2012; Adam et al., 2013). Further studies should provide models which simultaneously integrate multiple data sets. For example, the velocities anomalies provided by tomography models are used to derive temperature and density anomalies, which constitute the input of geodynamical models. The temperature and density anomalies should however be in agreement with the geochemical and petrological data. This aspect has been recently improved by the Perple_X software (Connolly, 2005), which integrates the latest results from mineral physics studies by incorporation of recent thermodynamic datasets (Stixrude and Lithgow-Bertelloni, 2011), and then provide more realistic geodynamical models. At the same time, geodynamical models should be able to accurately reproduce the observed depth and gravity anomalies, as well as other indicators of surface deformation such as the seismicity pattern, of the GPS velocity.

Geochemists have tried to answer address the question of what constitutes a deep mantle plume. Ocean Island Basalts appear to be enriched in noble gases when compared to Mid Oceanic Ridge Basalts (MORB). The traditional argument is that as mid-oceanic ridges sample a shallow part of the mantle, plumes must tap deep reservoirs, enriched in noble gases, which remained isolated from intermixing. However, recent studies indicate that there is no need to invoke deep isolated reservoirs to account for the geochemical signatures of OIB (Anderson, 1998; Allégre, 2002). In then appears that 'geochemistry will not deliver the silver bullet for proving or disproving plumes' (Hofmann and Hart, 2007).

Seismology seems to be the best prospect for directly imaging mantle plumes (e.g., Montelli et al., 2004, 2006; Wolfe et al., 2009); however this approach is not without problems (c.f., Julian, 2005). Most global tomographic models lack the resolution to image plumes and many regional studies lack sufficient crossing rays to resolve structures in the lower mantle. Theoretical developments continue to improve seismic methods. In the mean time, we had hoped that receiver functions and transition zone thickness would prove to be a more robust indicator of possible deep plume source (Li et al., 2003; Benoit et al., 2006; Deuss, 2007; Suetsugu et al., 2007; Lawrence and Shearer, 2008; Gu et al., 2009; Helffrich et al., 2010; Benoit et al., 2013). Given the scatter in the reported transition zone thicknness estimates, even for Hawaii, we see that there is significant room for improvement. We find at best a weak correlation between hotspot buoyancy flux and transition zone thickness, even when only considering the largest hotspots.

Even though Sleep's estimations of the buoyancy fluxes were made with observations that are more than 30 years old, they are still used in recent global studies because, until now, no newer global synthesis has been available. In addition to providing an updated global estimation of the buoyancy fluxes associated with hotspots, we emphasize the associated uncertainties in the buoyancy flux calculations, which are sometimes quite large, in spite of the improvement of the global data sets such as digital elevation and sediment thickness maps. For example, the estimation of the total heat flow associated with the swells and superswells varies from 1.67–2.23 TW, while varying the integration parameters. These variations could have significant implications when used as inputs to other quantitative models. When considering models of compressible mantle convection Leng and Zhong (2008), these estimates might indicate as little as 1/3 of the flux at the core-mantle boundary.

While we hope that this updated compilation will be useful to the earth science community, we hope that users will consider not only the values but the uncertainties when working with buoyancy fluxes. This is one reason we are providing all of our residual depth anomaly maps and profiles in the online supplement to allow readers to make their own evaluation of our measurements.

Acknowledgements

This work was supported by NSF grant EAR-0855446. We thank George Helffrich for helpful discussion on converting receiver function time delays to transition zone thickness and Shijie Zhong and Valerie Clouard for constructive reviews. We used GMT (Wessel and Smith, 1991) for figures and data analysis.

Albers, M. and Christensen, U., (1996), The excess temperature of plumes rising from the core-mantle boundary, *Geophys. Res. Lett.*, *23*, 3567–3570.

Adam C. and A. Bonneville (2009) No thinning of the lithosphere beneath the Cook-Austral chain, *J. Geophys. Res.*, *113*, B10104.

Adam, C., and A. Bonneville (2005), Extent of the South Pacific Superswell, *J. Geophys. Res.*, *110*, B09408.

Adam C, P. Madureira, J.M. Miranda, N. Lourenco, M. Yoshida, and D. Fitzenz (2013) Mantle dynamics and characteristics of the Azores plateau, *Earth Planet. Sci. Lett.*, *362*, 258–271.

Adam C., V. Vidal, M. Yoshida, T. Isse, D. Suetsugu, Y. Fukao, G. Barruol (2010), South Pacific hotspot swells dynamically supported by mantle flows, *Geophys. Res. Lett.*, *27*. L08302

Adam C., V. Vidal, and J. Escartn (2007) 80-Myr history of buoyancy and volcanic fluxes along the trails of the Walvis and St. Helena hotspots (South Atlantic), *Earth Planet. Sci. Lett.*, *261*, 432–442.

Adam C., V. Vidal, and A. Bonneville (2005), MiFil: A method to characterize seafloor swells with application to the south central Pacific, *Geochem. Geophys. Geosyst.*, *6*, Q01003.

Allégre C.J. (2002). The evolution of mantle mixing, *Philos. Trans. R. Soc. London*, *360*, 1–21.

Amante, C. and B. W. Eakins (2009) ETOPO1 1 Arc-Minute Global Relief Model: Procedures, Data Sources and Analysis. *NOAA Technical Memorandum NESDIS NGDC-24*, 19 pp, March 2009.

Anderson, D. L. (2005), Scoring hotspots: The plume and plate paradigms, in *Foulger, G.R. et al., Eds., Plates, plumes, and paradigms: Geological Society of America Special Paper 388*, p. 19-29.

Anderson, D. L., 2002. Plate Tectonics as a Far-From-Equilibrium Self-Organized System, in *AGU Monograph: Plate Boundary Zone, Geodynamics Series*, *30*, S. Stein and J. Freymuller, editors, p. 411–425.

Anderson, D. L., 2001, Top-Down Tectonics?, *Science*, *293*, 2016–2018.

Anderson, D. (1998).The Helium Paradoxes, *Proc. Natl. Acad. Sci. USA*, *95*, 4822–4827.

Benoit, M. H., M. D. Long, and S. D. King (2013) Anomalously thin transition zone and apparently isotropic upper mantle beneath Bermuda: Evidence for upwelling, *Geochem. Geophys. Geosyst. xxx*.

Ballmer, M.D., C.P. Conrad, E.I. Smith, and N. Harmon (2013), Non-hotspot volcano chains produced by migration of shear-driven upwelling toward the East Pacific Rise, Geology, 41, 479-482.

Benoit, M. H. A. A. Nyblade, T. J. Owens, G. Stuart (2006) Mantle transition zone structure and upper mantle S velocity variations beneath Ethiopia: Evidence for a broad, deep-seated thermal anomaly, *Geochem. Geophys. Geosyst.*, *7*, Q11013.

Bonneville, A., L. Dosso, and A. Hildenbrand (2006), Temporal evolution and geochemical variability of the South Pacific superplume activity, *Earth Planet. Sci. Lett.*, *244*, 251–269.

Bonneville, A., R. Le Suavé, L. Audin, V. Clouard, L. Dosso, P.-Y. Gillot, P. Janney, K. Jordahl, K. Maamaatuaiahutapu, (2002) Arago Seamount: The missing hotspot found in the Austral Islands, *Geology*, *30*, 1023–1026.

Boschi, L., T. W. Becker, and B. Steinberger (2007), Mantle plumes: Dynamic models and seismic images, *Geochem. Geophys. Geosyst.*, *8*, Q10006.

Brousse, R. and G. Barscus and H. Bellon and J.-M. Cantagrel and C. Diraison and H. Guilloi and C. Leotot, Variation in subsidence rates along intermediate and fast spreading mid-ocean ridges, *Bull. Soc. Géol. France*, *6*, 933–949, 1990.

Burke, K. (2011) Plate tectonics, the Wilson cycle, and mantle plumes: Geodynamics from the top, *Ann. Rev. Earth. Planet. Sci.*, *39*, 1-29.

Caress, D.W. and D.N. Chayes, New software for processing data from side-scan-capable multibeam sonars, Oceans'95: *Challenges of our changing global environment*, Washington DC, NY, USA, Marine Technology Soc., *MTS-IEEE*, vol. 2, 997–1000, 1995.

Caroff, M. and H. Guillou and M. Lamiaux and R.C Maury and G. Guille and J. Cotten, Assimilation of oceanic crust by hawaiitic and mugearitic magmas: An example for Eiao (Marquesas), *Lithos*, *46*, 235–258, 1999.

Connolly, J.A.D., (2005), Computation of phase equilibria by linear programming: a tool for geodynamic modeling and its application to subduction zone decarbonation, *Earth Planet. Sci. Lett.*,*236*, 524–541.

Crough, S. T. (1983), Hotspot Swells *Ann. Rev. Earth Planet. Sci.*, *11*, 165–193.

Crough, S. T. (1978) Thermal origin of mid-plate hot-spot swells, *Geophys. J. R. Astron. Soc.*, *55*, 451–469.

Courtier, A. M., M. G. Jackson, J. F. Lawrence, Z. Wang, C-T. Lee, et al. (2007) Correlation of seismic and petrologic thermometers suggests deep thermal anomalies beneath hotspots, *Earth Planet. Sci. Lett.*, *264*, 308–316.

Courtillot, V., A. Davaille, J. Besse, and J. Stock (2003), Three distinct types of hotspots in the Earth's mantle, *Earth Planet. Sci. Lett.*, *205*, 295–308.

Davies, G. F. (1988), Ocean Bathymetry and Mantle Convection; 1. Large-scale flow and hotspots, *J. Geophys. Res.*, *93*, 10,467–10,480.

Davies, G. F., and F. Pribac (1993), Mesozoic seafloor subsidence and the Darwin Rise, past and present, in *The Mesozoic Pacific, Geophys. Monogr. Ser., vol. 77*, edited by M. Pringle et al., pp. 39–52, AGU, Washington, D. C.

Desonie, D. and R. Duncan and J. Natland, (1993), Temporal and geochimical variability of volcanic products of the Marquesas hotspot, *J. Geophys. Res.*, *89*, 17649–17665.

Detrick, K. S. and Crough, S. T. (1978) Island subsidence, hot spots and lithospheric thinning, *J. Geophys. Res.*, *83*, 1236–1244.

Deuss, A. (2007) Seismic observations of transition-zone discontinuities beneath hotspot locations , *Special Papers of the Geological Society of America: Plates, Plumes and Planetary Processes*, *430*, 121–136

Diraison, C. (1991) Le volcanisme aérien des archipels polynésiens de la Société, des Marquises et des Australes-Cook, Ph.D. thesis, *Univ. de Bretagne Occidentale*, *413 p*.

Doin, M. P., and L. Fleitout (1996), The thermal evolution of the oceanic lithosphere: An alternative view, *Earth Planet. Sci. Lett., 142*, 121–136.

Douglass, J. and J.-G. Schilling and D. Fontigne, Plume-ridge interactions of the Discovery and Shona mantle plumes with the southern Mid-Atlantic ridge(40°), *J. Geophys. Res.*, *104*, 2941–2962, 1999.

Duncan, R.A. and I. McDougall, Migration of volcanism with time in the Marquesas Islands, French Polynesia, *Earth Planet. Sci. Lett.*, *21*, (4), 414–420, 1974.

Foulger, G.R. and D.L. Anderson (2005), A cool model for the Iceland hotspot: An origin for the Icelandic volcanic province in the remelting of subducted Iapetus slabs at normal mantle temperatures, *J. Volc. Geotherm. Res.*, *141*, 1–22.

Foulger, G.R., J.H. Natland and D.L. Anderson (2005) A source for Icelandic magmas in remelted Iapetus crust, *J. Volc. Geotherm. Res.*, *141*, 23–44.

Frost, D. J. (2008) The Upper Mantle and Transition Zone, *Elements*, *4*, 175–180.

Ghosh A., and W. E., Holt, 2012, Plate Motions and Stresses from Global Dynamic Models, Science, 335, 838-843

Gordon, R. G., and D. M. Jurdy (1986), Cenozoic global plate motions. *J. Geo phys. Res.*, *91*, 12,389–12,406.

Grégoire, M., M. Rabinowicz, and J. A. Janse (2006), Mantle Mush Compaction: a Key to Understand the Mechanisms of Concentration of Kimberlite Melts and Initiation of Swarms of Kimberlite Dykes, *J. Petrology*, *47*, 3, 631-646.

Gripp, A. E., and R. G. Gordon (2002), Young tracks of hotspots and current plate velocities. *Geophys. J. Int.*, *150*, 321–364.

Gripp, A. E., and R. G. Gordon (1990), Current plate velocities relative to the hopspots incorporating the NUVEL-1 global plate motion model. *Geophys. Res. Lett.*, *17*, 1109–1112.

Gu, J. Y., Y. An, M. Sacchi, R. Schultz, and J. Ritsema (2009) Mantle reflectivity structure beneath oceanic hotspots, *Geophys. J. Int.*, *178*, 1456–1472.

Gurnis, M., Mitrovica, J. X., Ritsema, J., and van Heijst, H.-J. (2000) Constraining mantle density structure using geological evidence of surface uplift rates: The case of the African superplume, *Geochem. Geophys. Geosys. 1*, 1020.

Hayes, D. E. (1988) Age-depth relationships and depth anomalies in the southeast Indian Ocean and South Atlantic Ocean, *J. Geophys. Res.*, *83*, 2937–2954.

Helffrich, G. (2000), Topography of the transition zone seismic discontinuities, *Rev. Geophys.*, *38*, 141–158.

Helffrich, G., B. Faria, J. F. B. D. Fonseca, A. Lodge and S. Kaneshima (2010) Transition zone structure under a stationary hot spot: Cape Verde, *Earth Planet. Sci. Lett.*, *289*, 156–161.

Hill, R.I., Campbell, I.H., Davies, G.F., and Griffiths, R.W., (1992), Mantle plumes and continental tectonics: *Science*, *256*, 186-193.

Hillier, J. K. (2010), Subsidence of normal seafloor: Observations do indicate flattening, *J. Geophys. Res.*, *115*, B03102.

Hillier, J. K., and A. B. Watts (2005), Relationship between depth and age in the North Pacific Ocean, *J. Geophys. Res.*, *110*, B02405.

Hillier, J., and Watts, A. (2004), "Plate-like" subsidence of the East Pacific Rise–South Pacific Superswell system, *J. Geophys. Res.*, *109*, B10102.

Hofmann, A. W., and Hart, S.R. (2007), Another nail in which coffin? *Science*,

315, 39-40.

Isse, T., D. Suetsugu, H. Shiobara, H. Sugioka, T. Kanazawa, and Y. Fukao (2006), Shear wave speed structure beneath the South Pacific superswell using broadband data from ocean floor and islands, *Geophys. Res. Lett.*, *33*, L16303.

Ito, G. and P. E. van Keken (2007), Hot spots and melting anomalies, in: *Treatise on Geophysics, Volume 7*, 371–435.

Ito, G., J. Lin, and C. Gable (1997) Interaction of mantle plumes and migrating mid-ocean ridges: Implications for the Galapagos plume-ridge system, *J. Geophys. Res.*, *102*, 15,403–15,417.

Jaupart, C., S. Labrosse, and J.-C. Mareschal (2007) Temperatures, heat and energy in the mantle of the Earth, *Treatise of Geophysics*, *Volume 7*, 253–304.

Julian, B. R. (2005), What can seismology say about hot spots?, in *Plates, Plumes, and Paradigms*, edited by G. R. Foulger, J.H. Natland, D.C. Presnall and D.L. Anderson, pp. 155-170, Geological Society of America.

Kerr, R. C. and C. Mériaux (2004) Structure and dynamics of sheared mantle plumes, *Geochem. Geophys. Geosyst.*, *5*, Q12009.

Kellogg, L.H., and S.D. King (1997), The effect of temperature dependent viscosity on the structure of new plumes in the mantle: Results of a finite element model in a spherical, axisymmetric shell, *Earth Planet. Sci. Lett.*, *148*, 13–26.

King, S. D. (2007), Hotspots and edge-driven convection, *Geology*, *35*, 223–226.

King, S.D. and D.L. Anderson (1998), Edge driven convection, *Earth Planet. Sci. Lett., 160*, 289–296.

King, S.D., and D.L. Anderson (1995) An alternative mechanism of flood basalt formation, *Earth Planet. Sci. Lett.*, *136*, 269–279.

King, S. D. and H. L. Redmond (2007), The structure of thermal plumes and geophysical observations, in Foulger, G.R., and Jurdy, D.M., eds., *Plates, plumes, and planetary processes: Geological Society of America Special Paper 430*, p. 103-120,

King, S. D., and J. Ritsema (2000) African hotspot volcanism: Small-scale convection in the upper mantle beneath cratons, *Science*, *290*, 1137–1140.

Korenaga, T., and J. Korenaga (2008), Subsidence of the oceanic lithosphere, apparent thermal expansivity, and seafloor flattening, *Earth Planet. Sci. Lett.*, *268*, 41–51.

Lawrence, J. F., and P. M. Shearer (2008) Imaging mantle transition zone thickness with SdS-SS finite-frequency sensitivity kernels, *Geophys. J. Int.*, *174*, 143–158.

Leng, W., and S. J. Zhong (2008), Controls on plume heat flux and plume excess temperature, *J. Geophys. Res.*, *113*, B04408.

Li, X., R. Kind and X. Yuan (2003) Seismic study of upper mantle and transition zone beneath hotspots, *Phys. Earth Planet. Inter.*, *136*, 79–92.

Lin, S-C. and P. E. van Keken (2006) Dynamics of thermochemical plumes: 2. Complexity of plume structures and its implications for mapping mantle plumes, *Geochem. Geophys. Geosyst.*, *7*, Q03003.

Malamud, B. D. and D. L. Turcotte (1999) How many plumes are there?, *Earth Planet. Sci. Lett.*, *174*, 113–124.

Mammerickx, J., and E. Herron (1980), Evidence for two fossil spreading ridges in the southeast Pacific, *Geol. Soc. Am. Bull.*, *91*, 263–271.

Marty, J. C., and A. Cazenave (1989), Regional variations in subsidence rate of oceanic plates: A global analysis, *Earth Planet. Sci. Lett.*, *94*, 301–315.

McNutt, M. (1998), Superswells, *Rev. Geophys.*, *36*, 211–244.

McNutt, M. K. and A. Bonneville, A shallow, chemical origin for the Marquesas swell, *Geochim. Geophys. Geosyst.*, *1*, 1999GC000028, 2000.

McNutt, M. K., and K. Fischer (1987), The South Pacific Superswell, in *Seamounts, Islands, and Atolls*, Geophys. Monogr. Ser., vol. 43, edited by B. H. Keating et al., pp. 25–34, AGU, Washington, D. C.

McNutt, M. K., and L. Shure (1986) Estimating the compensation depth of the Hawaiian swell with linear filters, *J. Geophys. Res.*, *91*, 13,915–13,923.

McNutt M. K., K. Fischer, S. Kruse and J. H. Natland (1989) The origin of the Marquesas fracture zone ridge and its implications for the nature of hot spots, *Earth Planet. Sci. Lett.*, *91*, 381–393.

McNutt, M., Sichoix, L., and Bonneville, A. (1996). Modal depths from shipboard bathymetry: There is a South Pacific Superswell, *Geophys. Res. Lett.*, *23*, 3397– 3400.

Menard, H. W. (1973). Depth anomalies and the bobbing motion of drifting islands. *J. Geophys. Res. 78*, 28–37.

Minster, J. B. and T. H. Jordan (1978) Present day plate motions, *J. Geophys. Res.*, *83*, 5331–5354.

Montelli, R., G. Nolet, F. A. Dahlen, and G. Masters (2006) A catalogue of deep mantle plumes: New results from finite- frequency tomography, *Geochem. Geophys. Geosyst.*, *7*, Q11007.

Montelli, R., Nolet, G., Dahlen, F.A., Masters, G., Engdahl, E.R. and Hung, S.-H. (2004) Finite frequency tomography reveals a variety of plumes in the mantle, *Science*, *303*, 338–343.

Morgan, W.J. (1983), Hotspot tracks and the early rifting of the Atlantic, *Tectonophys.*, *94*, 123- 139.

Morgan, W. J. (1971), Plate motions and deep mantle convection, *Nature*, *230*, 42, 1971.

Morgan, W. J., and Phipps Morgan, J. (2007) Plate velocities in hotspot reference frame, in *Foulger, G.R., and Jurdy, D. M., eds.*, Plates, Plumes, and Planetary Processes, *Geol. Soc. Amer. Special Paper 430*, p. 65-78.

Müller, R .D., M. Sdrolias, C. Gaina, and W. R. Roest (2008) Age, spreading rates and spreading symmetry of the world's ocean crust, *Geochem. Geophys. Geosyst.*, *9*, Q04006,

Parker, R., and D. Oldenburg (1973), Thermal model of ocean ridges, *Nature Phys. Sci.*, *242*, 137–139.

Parsons, B. and J. G. Sclater (1977) An Analysis of the variation of ocean floor bathymetry and heat flow with age, *J. Geophys. Res.*, *82*, 803–827.

Phipps Morgan, J. (1997) The generation of compositional lithsophere by mid-ocean ridge melting and its effect on the subsequent off-axis hotspot upwelling and melting, *Earth Planet. Sci. Lett.*, *146*, 213–232.

Pollack, H. N., I. G. Glass, R. S. Thorpe and D. S. Chapman (1981), On the vulnerability of lithospheric plates to mid-plate volcanism: Reply to comments by P. R. Vogt, *J. Geophys. Res.*, *86*, 961–966.

Pollitz, F. F., Pliocene change in the Pacific plate motion, *Nature*, *320*, 738–741, 1986.

Ribe, N. M. and U. R. Christensen (1999) The dynamical origin of Hawaiian hotspot volcanism, *Earth Planet. Sci. Lett.*, *171*, 517–531.

Ribe, N. M., and U. R. Christensen (1994), Three-dimensional modeling of plume-lithosphere interaction, *J. Geophys. Res.*, *99*, 669–682.

Richards, M. A. R. A. Duncan, and V. E. Courtillot (1989) Flood basalts and hotspot tracks: Plume heads and tails, *Science*, *246*, 103–107.

Schlanger, S., Garcia, M., Keating, B., Naughton, J., Sager, W., Haggerty, J. Philipotts, J., and Duncan, R. (1984), Geology and geochronology of the Line Islands, *J. Geophys. Res.*, *89*, 11,216–11,272.

Sclater, J., and J. Francheteau (1970), The implication of terrestrial heat flow observations on current tectonic and geochemical models of the crust and upper mantle of the Earth, *Geophys. J. R. Astron. Soc.*, *20*, 509–542.

Sichoix, L., Bonneville, A., and McNutt, M. (1998), The seafloor swells and superswell in French Polynesia, *J. Geophys. Res.*, *103*, 27,123–27,133.

Sleep, N. H. (1992), Hotspot volcanism and mantle plumes, *Annu. Rev. Earth Planet. Sci.*, *20*, 19–43.

Sleep, N. H. (1990), Hotspots and Mantle Plumes: Sume Phenomenology, *J. Geophys. Res.*, *95*, 6715–6936.

Stein, C. and S. Stein (1992) A model for the global variation in oceanic depth and heat flow with lithospheric age, *Nature*, *359*, 123–128.

Steinberger, B. (2000), Plumes in a convecting mantle: Models and observations for individual hotspots, *J. Geophys. Res.*, *105*, 11,127–11,152.

Steinberger, B. and R.J. O'Connell (1998), Advection of plumes in mantle flow: Implications for hotspot motion, mantle viscosity and plume distribution, *Geophysical J. Int.*, *132*, 412–434.

Stixrude L., and C. Lithgow-Bertelloni, (2011), Thermodynamics of mantle minerals II. Phase equilibria, *Geophys. J. Int.*, *184*, 1180-1213.

Stuart, W. D., G. R. Foulger, and M. Barall (2007) Propagation of the Hawaiian-Emperor volcano chain by Pacific plate cooling stress, in *Foulger, G.R., and Jurdy, D. M., eds.*, Plates, Plumes, and Planetary Processes, *Geol. Soc. Amer. Special Paper 430*, p. 497–506.

Suetsugu, D., Shiobara, H., Sugioka, H., Fukao, Y., Kanazawa, T. (2007) Topography of the mantle discontinuities beneath the South Pacific superswell as inferred from broadband waveforms on seafloor, *Phys. Earth Planet. Inter.*, *160*, 310–318.

Tucholke, B.E., and P.R. Vogt (1979), Western North Atlantic: Sedimentary evolution and aspects of tectonic history, in Tucholke, B.E. and P.R. Vogt, eds., Initial Reports of the Deep Sea Drilling Project, v. 43, U.S. Govt. Printing Office, Washington, D.C., 791–825.

Turcotte, D.L. and G. Schubert, *Geodynamics*, 2^{nd} edition, Cambridge Univ. Press, pp. 456.

Turcotte, D.L. and E.R. Oxburgh (1973) Mid-plate tectonics, *Nature*, *244*, 337–339.

Turcotte, D.L. and E.R. Oxburgh (1967) Finite amplitude convective cells and continental drift, *J. Fluid Mech.*, *28*, 29–42.
Van Wykhouse, R. (1973). SYNBAPS, Tech. Rep. TR-233, Natl. Oceanogr. Off., Washington, D. C.
Vidal, V., and A. Bonneville (2004), Variations of the Hawaiian hot spot activity revealed by variations in the magma production rate, *J. Geophys. Res.*, *109*, B03104.
Vogt, P. R. (1991) Bermuda and Appalachian-Labrador rises, *Geology*, *19*, 41–44.
Vogt, P. R. and W.-Y. Jung (2007), Origin of the Bermuda volcanoes and the Bermuda rise: History, observations, models, and puzzles, in *Foulger, G.R., and Jurdy, D.M., eds., Plates, plumes, and planetary processes: Geological Society of America Special Paper 430*, p. 553–591.
Wessel, P. (1993), Observational constraints on models of the Hawaiian hot spot swell, *J. Geophys. Res.*, *98*, 16,095–16,104.
Wessel, P., and W. H. F. Smith (1991) Free software helps map and display data, *EOS Trans. AGU*, *72*, 441–446.
White, W. M. (2010), Ocean island basalts and mantle plumes: The geochemical perspective, *Ann. Rev. Earth. Planet. Sci.*, *38*, 133-160.
Whittaker, J., A. Goncharov, S. Williams, R. D. Müller, G. Leitchenkov (2013) Global sediment thickness dataset updated for the Australian-Antarctic Southern Ocean, *Geochem. Geophys. Geosys.. 10*.
Wilson, J. T. (1963), A possible origin of the Hawaiian Islands, *Can. J. Phys.*, *41*, 863–870.
Wolfe et al. (2009) Mantle Shear-Wave Velocity Structure Beneath the Hawaiian Hot Spot, Science, 326, 1388–1390.
Wolfe, C.J. and M.K. McNutt and R.S. Detrick, The Marquesas archipelagic apron: Seismic stratigraphy and implications for volcano growth, mass wasting and crustal underplating, *J. Geophys. Res.*, *99*, 13591–13608, 1994.

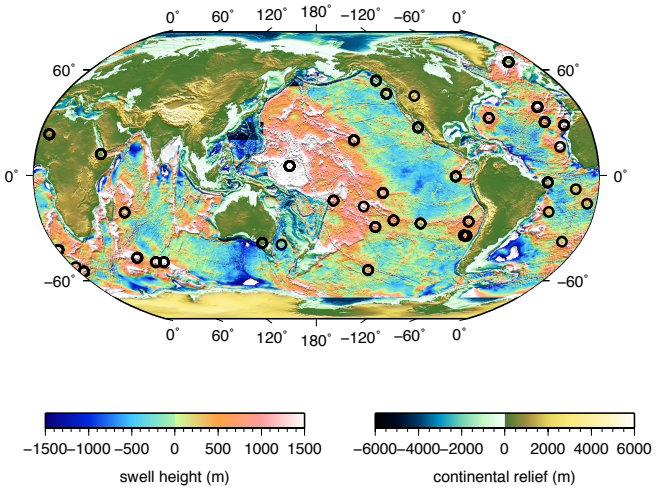

Figure 1: Residual depth anomaly taking ETOPO1 and removing a square root of age bathymetry and sediment thickness using Whittaker et al. (2013). The circles are locations of the hotspots described by Sleep (1990).

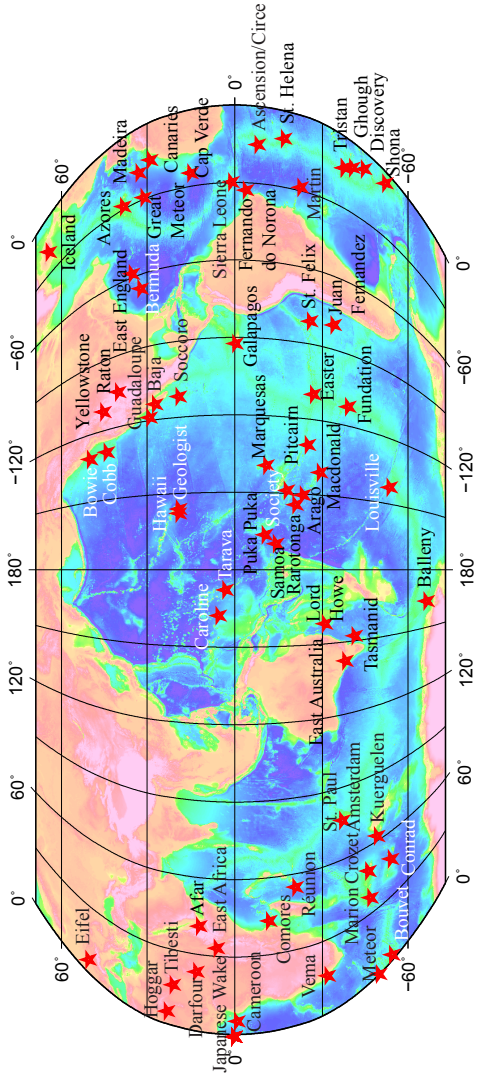

Figure 2: Location of Hotspots taken from Table 1.

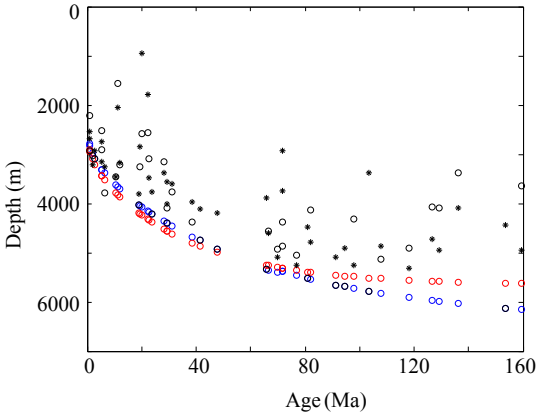

Figure 3: Mean depth. The red and blue circles describe the depth predicted by the GDH1 (Stein and Stein, 1992) and PSM (Parsons and Sclater, 1977) models respectively. The black circles and stars, the mean depth estimated with the MiFil and Geometrical methods respectively.

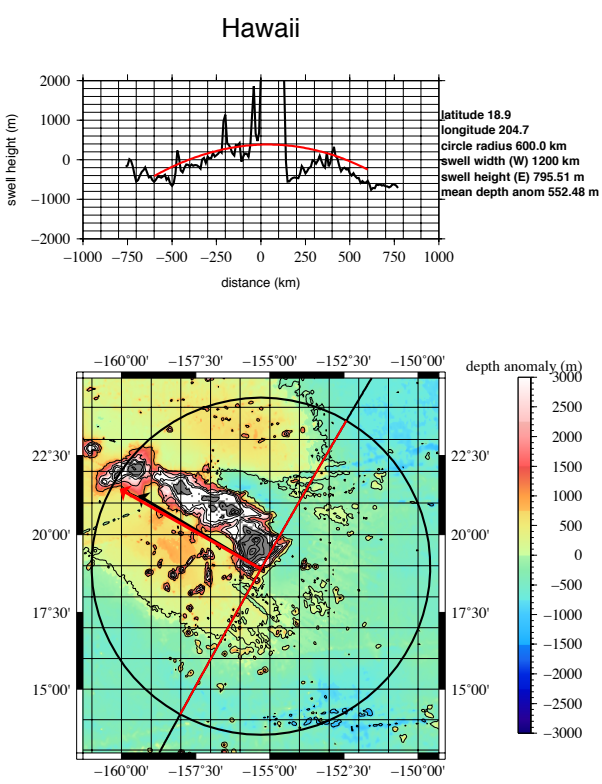

Figure 4: (below) Residual depth anomaly map for Hawaii using the geometry method discussed in the text. (Above) Cross-section of the residual depth anomaly perpendicular to the HS3-Nuvel1A plate velocity at Hawaii (black line) illustrating the measurement of swell width and height. A quadratic surface fit to the residual depth anomaly using the GMT routine *grdtrend* is shown in red. This fit is used to aid the eye in determining the swell height, although not all hotspot swells fit this simple trend.

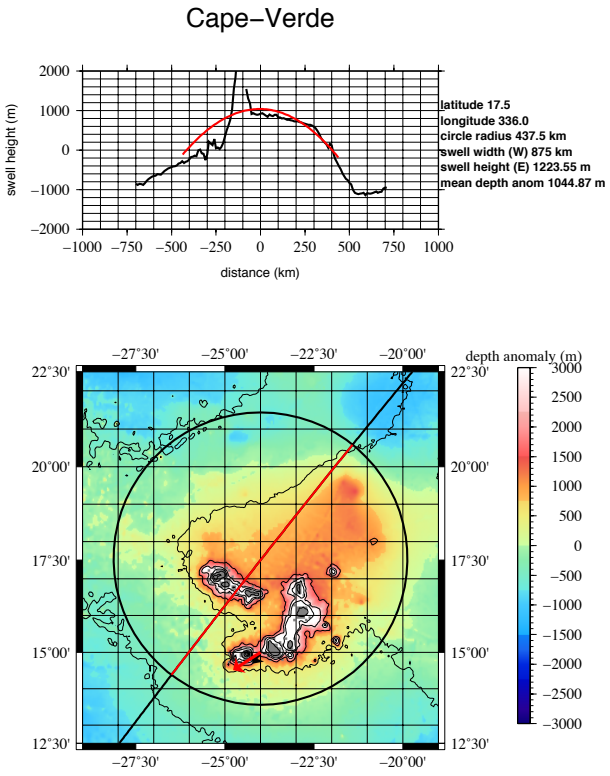

Figure 5: (below) Residual depth anomaly map for Cape Verde using the geometry method discussed in the text. The black circle is a radius of 800 km centered on the center of the swell. (Above) Cross-section of the residual depth anomaly parallel to the HS3-Nuvel1A plate velocity at Cape Verde (black line) illustrating the measurement of swell width and height. A quadratic surface fit to the residual depth anomaly using the GMT routine *grdtrend* is shown in red. This fit is used to aid the eye in determining the swell height, although not all hotspot swells fit this simple trend.

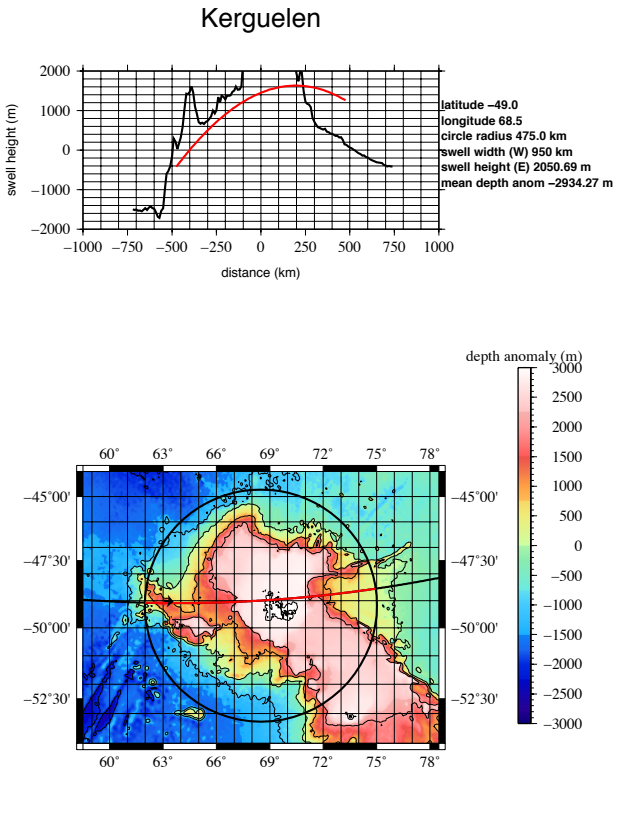

Figure 6: (below) Residual depth anomaly map for Kerguelen using the geometry method discussed in the text. The black circle is a radius of 800 km centered on the center of the swell. (Above) Cross-section of the residual depth anomaly perpendicular to the HS3-Nuvel1A plate velocity at Kerguelen (black line) illustrating the measurement of swell width and height. A quadratic surface fit to the residual depth anomaly using the GMT routine *grdtrend* is shown in red. This fit is used to aid the eye in determining the swell height, although not all hotspot swells fit this simple trend.

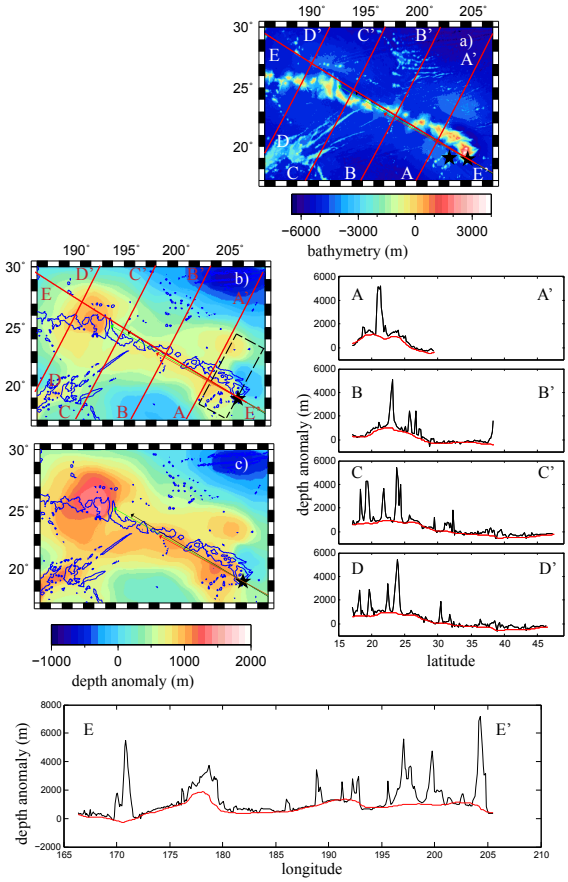

Figure 7: Hawaii: bathymetry (a) and depth anomaly (b) and(c). The depth anomaly has been computed through the MiFil method using the GDH1 and the PSM models, respectively in panels b) and c). In panel b), we also report in black dashed line, the box in which we integrated the swell volume. The arrows represent the plate's velocity provided the kinematics models. In the hotspot referential we considered the HS3-nuvel1 and HS2-nuvel1, respectively in green and red. In the no-net-rotation, we have considered the HS3-nuvel1 model in black.

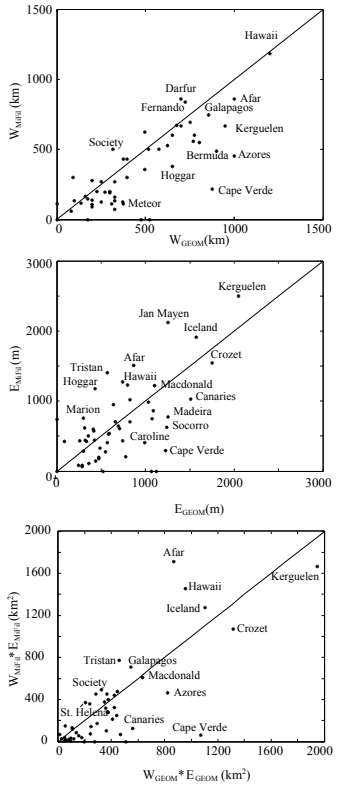

Figure 8: Measurements of swell a) width and b) elevation from MiFil versus Geometrical method for the hotspots listed in Table 2.

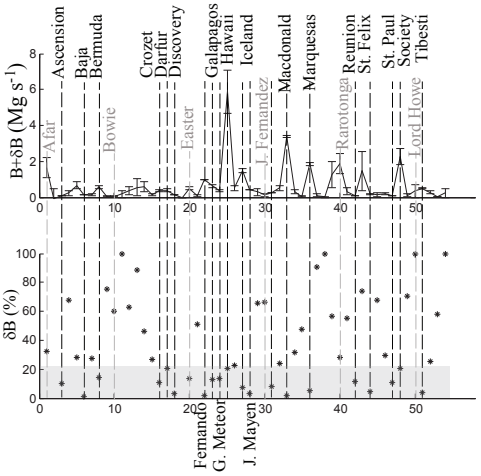

Figure 9: Average buoyancy flux using Geometrical and MiFil-area methods with HS3-Nuvel1a for plate velocity. Error bars determined calculating the difference in cross-sectional area for the two methods (Table 3). The hotspots are listed in alphabetical order along the x-axis.

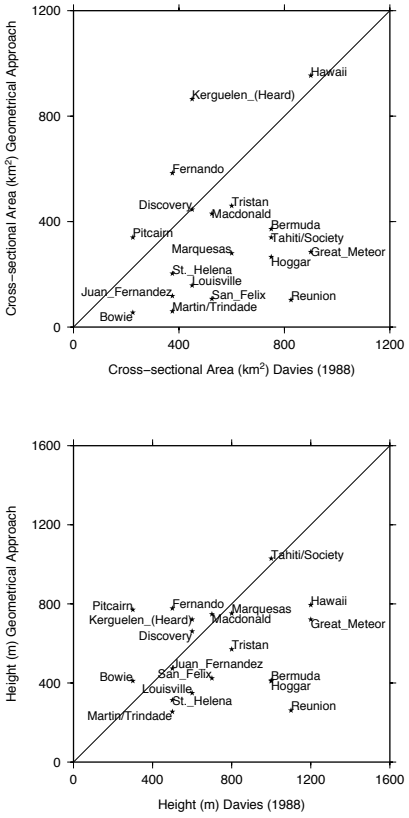

Figure 10: a) Measurements of swell a) width and b) height measured using the Geometry approach versus Davies (1988) for the hotspots listed in Table 2.

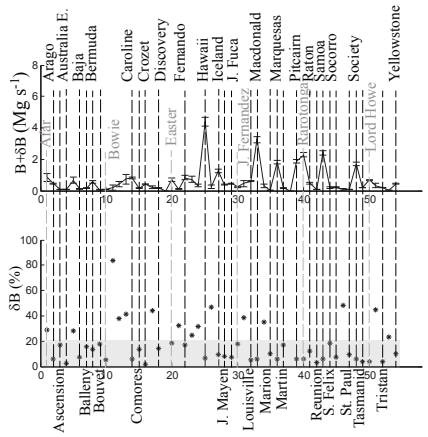

Figure 11: Buoyancy flux calculated using the Geometrical method. The error bars are determined by conisdering the difference between the HS2-Nuvel1a and HS3-Nuvel1a plate velocity for each hotspot listed in Table 2. The hotspots are listed in alphabetical order along the x-axis.

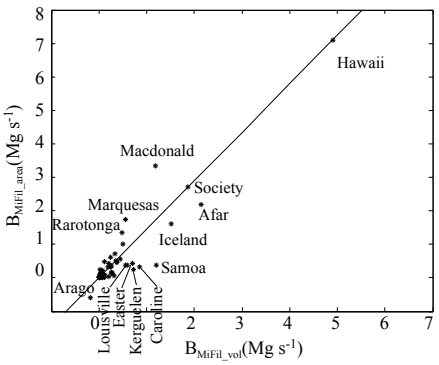

Figure 12: Buoyancy flux calculated from the MiFil approach using the volume versus the cross-sectional area method for the hotspots listed in Table 2.

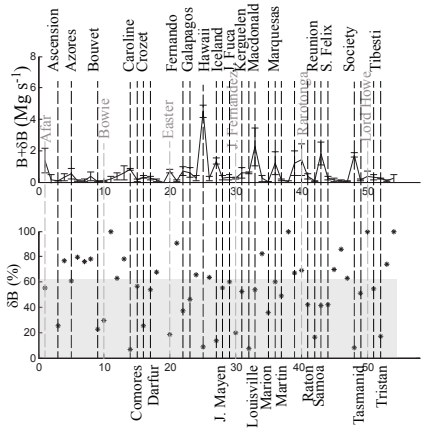

Figure 13: Buoyancy flux computed through the three approaches described in the text. The error bars are determined using both the difference between the HS2-Nuvel1a and HS3-Nuvel1a plate velocity, and the swells' determination (volume integration versus cross-sectional areas) for each hotspot listed in Table 2. The hotspots are listed in alphabetical order along the x-axis.

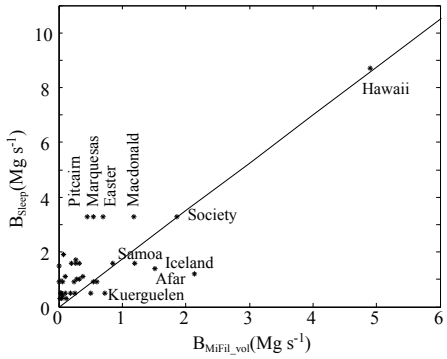

Figure 14: Buoyancy flux calculated from the MiFil approach using the volume versus area methods Sleep (1990) for the hotspots listed in Table 2.

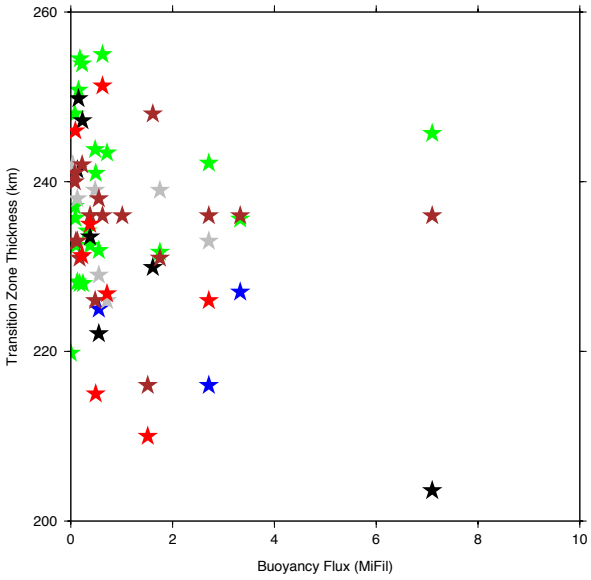

Figure 15: Transition zone thickness from seismic observations compared with MiFil buoyancy flux. Green stars are from (Deuss, 2007), black stars are from (Li et al., 2003), blue stars are from (Suetsugu et al., 2007), grey stars are from (Lawrence and Shearer, 2008), brown stars are from (Gu et al., 2009), and red stars are from (**????**Benoit et al., 2006; Helffrich et al., 2010; Benoit et al., 2013).

Table 1: Hotspot Lists Comparison

Hotspot Name	Longitude	Latitude	Davies (1988)	Sleep (1990)	Steinberger (2000)	Courtillot et al. (2003)	Anderson (2005)	Ito & van Keken (2007)	White (2011)
Afar/Ethiopia	42	12[1]	X	X		X	X	X	
Arago	209.3	-23.5[3]						X	
Ascenscion	346.0	-8.0[1]	X			X	X	X	
Australia, East	143	-38[1]		X			X	X	
Azores	332	38[1]			X	X	X	X	X
Baja/Guadalupe	247	27[1]		X	X	X	X	X	
Balleny	164.7	-67.4[1]			X	X	X	X	X
Bermuda	295	32[1]	X	X		X	X	X	
Bouvet	3.4	-54.4[1]		X		X	X	X	X
Bowie	230	49.5[1]	X		X	X	X	X	
Cameroon	6.0	-1[1]			X	X	X	X	
Canary	343	28[1]		X	X	X	X	X	X
Cape Verde	336	15[1]	X	X	X	X	X	X	
Caroline	163	5.3[1]		X		X	X	X	
Comores	44	-12[1]			X	X	X	X	
Crozet/Prince Edward	50	-46[1]				X	X	X	X
Darfur	24	13[1]	X		X	X	X	X	
Discovery	353.5	-44.5[1]	X	X		X	X	X	
East Africa	34	6[1]	X		X		X	X	
Easter Island	251	-27[1]			X	X	X	X	X
Eifel	7	50[1]			X	X	X	X	
Fernando	328	-4[1]	X	X	X	X	X	X	
Galapagos	268	-0.4[1]		X	X	X	X	X	X
Great Meteor/New England	331.5	31[1]	X	X	X	X	X	X	
Hawaii	204.7	18.9[1]	X	X	X	X	X	X	X
Hoggar	6	23[2]	X	X	X	X	X	X	
Iceland	342.4	64.6[1]		X	X	X	X	X	X
Jan Mayen	352	71.7[1]			X	X	X	X	
Juan de Fuca/Cobb	231.3	43.6[1]		X	X	X	X	X	
Juan Fernandez	281	-34[1]	X	X	X	X	X	X	
Kerguelen (Heard)	63	-49[1]	X	X	X	X	X	X	X
Louisville	218.8	-53.5[1]	X	X	X	X	X	X	
Macdonald /Austral Cook	219.6	-29[3]	X	X	X	X	X	X	
Madeira	342.5	32.7[1]					X	X	
Marion	37.75	-46.75[1]			X	X	X	X	
Marquesas	222.5	-11.5[3]	X	X	X	X	X	X	X
Martin/Trindade	331	-20[2]	X	X	X	X	X	X	X
Meteor	1	-52[2]		X	X	X	X	X	
Pitcairn	230.7	-25.3[3]	X	X	X	X	X	X	
Rarotonga	200.3	-21.5[3]					X	X	X
Ratan	256	37[2]			X	X	X		
Reunion	55.5	-21[1]	X	X	X	X	X	X	X
Samoa	191	-14.3[1]		X	X	X	X	X	X
San Felix	280	-26[1]	X	X	X	X	X	X	X
Socorro	249	19[1]			X	X	X	X	
St. Helena	350	-17[1]	X	X	X	X	X	X	
St. Paul-Amsterdam	78	-37[1]					X	X	
Tahiti/Society	212	-18.3[3]	X	X	X	X	X	X	
Tasman, Central/Tasminid	153	-41.2[1]	X		X	X	X	X	
Tasman, East/Lord Howe	159	-31[1]		X		X	X	X	
Tibesti	17	21[1]	X		X	X	X	X	
Tristan	350	-40.3[1]	X		X	X	X	X	
Vema	16	-32[1]	X		X	X	X	X	
Yellowstone	249	44.8[1]		X	X	X	X	X	

[1] Ito and van Keken (2007)
[2] Courtillot et al. (2003)
[3] Adam et al. (2010)

Table 2: Hotspot locations and buoyancy fluxes from Davies (1988) and Sleep (1990).

Hotspot Name	Latitude	Longitude	Mass Flux (Mg s^{-1})		Reliabi
			Sleep	Davies	
Afar	7	39.5	1.2		goo
Australia	-38	143	0.9		fair
Azores	37.9	334	1.1		fair
Baja/Guadalupe	27.7	245.5	0.3		poo
Bermuda	32.6	295.7	1.1	1.5	goo
Bouvet	-54.4	3.4	0.4		fair
Bowie	53	225.2	0.3	0.8	poo
Canary	28.2	342	1.0		fair
Cape Verde	16	336	1.6	0.5	goo
Caroline	5.3	163	1.6		poo
Crozet/Pr.Edward	-46.1	50.2	0.5		goo
Discovery	-43	357.3	0.5	0.4	poo
Easter	-27	251	3.3		fair
Fernando	-4	328	0.5	0.9	poo
Galapagos	-0.4	268.4	1.0		fair
Great Meteor	29.4	331.8	0.5	0.5	poo
Hawaii	18.9	204.7	8.7	6.2	goo
Hoggar	23.3	5.6	0.9	0.4	fair
Iceland	64.4	342.7	1.4		goo
Juan de Fuca/Cobb	46	229.9	0.3		fair
Juan Fernandez	-33.9	278.2	1.6	1.7	poo
Kerguelen (Heard)	-49.6	69	0.5	0.2	poo
Louisville	-53.55	218.8	0.9	3.0	poo
Macdonald	-29	219	3.3	3.9	fair
Marquesas	-10	222.5	3.3	4.6	fair
Martin/Trindade	-20	331	0.5	0.8	poo
Meteor	-52	1	0.5	0.4	poo
Pitcairn	-25.5	230.7	3.3	1.7	fair
Reunion	-21.2	55.7	1.9	0.9	goo
St. Helena	-16.5	350.5	0.5	0.3	poo
Samoa	-14.3	191	1.6		poo
San Felix	-26	280	1.6	2.3	poo
Tahiti/Society	-18.3	212	3.3	5.8	fair
Tasman, Central/Tasmantid	-40.4	155.5	0.9		poo
Tasman, East/Lord Howe	-34.7	159.8	0.9		poo
Tristan	-37.2	347.7	1.7	0.5	fair
Yellowstone	44.5	249.6	1.5		fair

Table 3: Hotspot buoyancy fluxes from this study. Buoyancy fluxes calculated using the HS3-Nuvel1a reference frame. MiFil method fluxes calculated using cross-sectional area times plate and using volume and age of volcanism. See text for details.

	Geometrical			MiFil area			MiFil volume
Hotspot Name	W (km)	E (m)	Bflux (Mg s^{-1})	W (km)	E (m)	Bflux (Mg s^{-1})	Bflux (Mg s^{-1})
Afar	1000.	869.11	1.11	859.64	1505.80	2.18	2.14
Arago	90.	993.26	0.49	298.00	410.00	-0.60	-0.18
Ascension	100.	487.72	0.11	135.53	324.00	0.09	0.11
Australia, East	160.	84.23	0.08	164.74	423.48	0.39	0.55
Azores	1000.	823.40	0.85	453.13	1020.00	0.48	0.38
Baja	80.	320.89	0.13	58.65	444.27	0.13	0.01
Balleny	300.	825.57	0.19	198.22	700.00	0.11	0.04
Bermuda	900.	414.86	0.66	489.54	570.43	0.49	0.11
Bouvet	200.	435.64	0.06	87.52	140.18	0.01	0.06
Bowie	135.	410.41	0.07	115.97	600.27	0.02	0.05
Cameroon	475.	1067.50	0.37	0.00	0.00	0.00	0.00
Canaries	370.	1507.62	0.57	124.63	1026.40	0.13	0.29
Cape Verde	875.	1223.55	1.05	215.99	291.61	0.06	0.32
Caroline	200.	779.56	0.86	279.56	206.75	0.32	0.85
Comores	270.	1091.34	0.18	193.00	858.00	0.11	0.07
Crozet	750.	1755.76	0.40	691.88	1543.00	0.33	0.25
Darfur	700.	338.35	0.29	858.00	421.00	0.45	0.38
Discovery	675.	661.96	0.16	672.00	707.00	0.17	0.04
East Africa	0.	0.00	0.00	0.00	0.00	0.00	0.00
Easter	625.	590.87	0.56	525.00	540.00	0.43	0.70
Eifel	310.	300.00	0.12	111.30	281.00	0.04	0.01
Fernandodo	725.	584.53	0.96	838.00	530.00	1.00	0.51
Galapagos	855.	636.18	0.54	746.00	949.00	0.71	0.33
Great Meteor	395.	1072.56	0.44	432.00	750.00	0.33	0.18
Hawaii	1200.	795.51	4.66	1182.70	1228.40	7.10	4.90
Hoggar	650.	434.62	0.39	378.10	1.18	0.62	0.25
Iceland	700.	1575.65	1.40	668.73	1907.00	1.61	1.52
Jan Mayen	300.	1255.66	0.41	188.10	2120.00	0.44	0.21
Juan de Fuca	325.	549.85	0.48	133.60	274.62	0.10	0.12
Juan Fernandez	250.	473.53	0.19	123.15	193.07	0.04	0.20
Kerguelen	950.	2050.69	0.28	667.04	2495.80	0.24	0.73
Louisville	375.	357.19	0.63	430.47	500.36	0.38	0.60
Macdonald	575.	1099.69	3.45	500.00	1220.00	3.33	1.18
Madeira	325.	1252.47	0.42	268.91	774.00	0.22	0.08
Marion	175.	302.27	0.02	146.01	758.00	0.07	0.01
Marquesas	515.	693.39	1.96	500.00	640.00	1.75	0.55
Martin	325.	284.43	0.20	72.00	63.00	0.01	0.11
Meteor	0.	0.00	0.00	113.36	739.60	0.02	0.03
Pitcairn	770.	471.66	2.01	555.60	180.47	0.55	0.45
Rarotonga	775.	570.12	2.41	600.00	410.00	1.34	0.49
Raton	325.	741.05	0.51	159.78	433.00	0.15	0.26
Reunion	395.	261.92	0.06	298.71	434.44	0.08	0.07
Samoa	375.	1242.78	2.56	111.70	625.17	0.38	1.20
San Felix	250.	428.48	0.16	267.94	439.77	0.18	0.27
Socorro	200.	286.40	0.22	137.28	83.50	0.04	0.05
St. Helena	650.	313.72	0.13	600.00	620.00	0.23	0.03
St. Paul	495.	741.30	0.07	357.50	1268.30	0.09	0.02
Society	315.	1030.01	1.79	500.00	980.00	2.72	1.86
Tasmantid	200.	245.07	0.19	106.39	80.33	0.03	0.06
Lord Howe	175.	1119.86	0.71	0.00	0.00	0.00	0.00
Tibesti	495.	707.08	0.47	625.00	606.00	0.51	0.35
Tristan	805.	571.14	0.21	550.00	1400.00	0.35	0.27
Vema	225.	364.32	0.02	197.00	111.00	0.00	0.07
Yellowstone	525.	519.37	0.49	0.00	0.00	0.00	0.00

Table 4: Plate velocities from various plate models at select hotspots.

Hotspot	Reference	magnitude (mm yr^{-1})	orientation (degrees E of N)
Afar	HS2	9.58	341.72
Afar	HS3	17.67	286.65
Bouvet	HS2	10.80	166.06
Bouvet	HS3	15.49	201.46
Cape Verde	HS2	8.87	215.90
Cape Verde	HS3	21.06	237.26
Crozet	HS2	6.80	118.06
Crozet	HS3	6.46	193.73
Hawaii	GJ	86	
Hawaii	P81	96	
Hawaii	HS2	92	300.9
Hawaii	HS3	104.3	299.5
Kerguelen	HS2	6.96	84.73
Kerguelen	HS3	1.65	152.60
Reunion	HS2	12.40	9.43
Reunion	HS3	13.10	314.08
St. Helena	HS2	4.51	141.15
St. Helena	HS3	13.45	232.49
San Felix	HS2	46.59	82.53
San Felix	HS3	31.91	80.05

GJ - (Gordon and Jurdy, 1986)
P81 (Pollack et al., 1981)
HS2 - (Gripp and Gordon, 1990)
HS3 - (Gripp and Gordon, 2002)